Nuclear 11.3 μm PAH emission in local active galactic nuclei

A. Alonso-Herrero,[1][*][†] C. Ramos Almeida,[2,3][‡] P. Esquej,[4] P. F. Roche,[5]
A. Hernán-Caballero,[1] S. F. Hönig,[6][§] O. González-Martín,[2,3] I. Aretxaga,[7]
R. E. Mason,[8] C. Packham,[9] N. A. Levenson,[10] J. M. Rodríguez Espinosa,[2,3]
R. Siebenmorgen,[11] M. Pereira-Santaella,[12,13] T. Díaz-Santos,[14] L. Colina,[13]
C. Alvarez[2,3] and C. M. Telesco[15]

[1]*Instituto de Física de Cantabria, CSIC-UC, E-39005 Santander, Spain*
[2]*Instituto de Astrofísica de Canarias (IAC), E-38205 La Laguna, Tenerife, Spain*
[3]*Departamento de Astrofísica, Universidad de la laguna (ULL), E-38206 La Laguna, Tenerife, Spain*
[4]*Departamento de Astrofísica, Universidad Complutense de Madrid, E-28040 Madrid, Spain*
[5]*Department of Physics, University of Oxford, Oxford OX1 3RH, UK*
[6]*Dark Cosmology Centre, Niels Bohr Institute, University of Copenhagen, DK-2100 Copenhagen Ø, Denmark*
[7]*Instituto Nacional de Astrofísica, Optica y Electrónica (INAOE), 72000 Puebla, Mexico*
[8]*Gemini Observatory, Northern Operations Center, Hilo, HI 96720, USA*
[9]*Department of Physics and Astronomy, University of Texas at San Antonio, San Antonio, TX 78249, USA*
[10]*Gemini Observatory, Casilla 603, La Serena, Chile*
[11]*European Southern Observatory, D-85748 Garching b. München, Germany*
[12]*Istituto di Astrofisica e Planetologia Spaziali, INAF, I-00133 Roma, Italy*
[13]*Centro de Astrobiología, CSIC-INTA, E-28850 Torrejón de Ardoz, Madrid, Spain*
[14]*Spitzer Science Center, Caltech, Pasadena, CA 91125, USA*
[15]*Department of Astronomy, University of Florida, Gainesville, FL 32611, USA*

ABSTRACT

We present Gran Telescopio CANARIAS CanariCam 8.7 μm imaging and 7.5–13 μm spectroscopy of six local systems known to host an active galactic nucleus (AGN) and have nuclear star formation. Our main goal is to investigate whether the molecules responsible for the 11.3 μm polycyclic aromatic hydrocarbon (PAH) feature are destroyed in the close vicinity of an AGN. We detect 11.3 μm PAH feature emission in the nuclear regions of the galaxies as well as extended PAH emission over a few hundred parsecs. The equivalent width (EW) of the feature shows a minimum at the nucleus but increases with increasing radial distances, reaching typical star-forming values a few hundred parsecs away from the nucleus. The reduced nuclear EWs are interpreted as due to increased dilution from the AGN continuum rather than destruction of the PAH molecules. We conclude that at least those molecules responsible for the 11.3 μm PAH feature survive in the nuclear environments as close as 10 pc from the AGN and for Seyfert-like AGN luminosities. We propose that material in the dusty tori, nuclear gas discs, and/or host galaxies of AGN is likely to provide the column densities necessary to protect the PAH molecules from the AGN radiation field.

Key words: galaxies: active – galaxies: individual: Mrk 1066 – galaxies: individual: Mrk 1073 – galaxies: individual: NGC 2273 – galaxies: individual: Arp 299 – galaxies: individual: NGC 6240 – galaxies: individual: IRAS 17208−0014 – galaxies: Seyfert – infrared: galaxies.

1 INTRODUCTION

The fuelling of active galactic nuclei (AGN) requires that material be driven inwards from the interstellar medium of the host galaxy to physical scales of less than 1 pc (see the review by Alexander & Hickox 2012, and references therein). Therefore, nuclear ($<$100 pc regions) star formation appears to be an inevitable consequence of

[*] Augusto G. Linares Senior Research Fellow.
[†] E-mail: aalonso@ifca.unican.es
[‡] Marie Curie Fellow.
[§] Marie Curie Fellow.

this process. Indeed, numerical simulations predict that in AGN star formation in the nuclear region should be tightly correlated with the black hole accretion rate (e.g. Kawakatu & Wada 2008; Hopkins & Quataert 2010). Moreover, nuclear star formation via stellar feedback (stellar winds and supernovae) might help sustain the vertical thickness of the optically and geometrically thick dusty torus of the AGN unified model (see e.g. Wada & Norman 2002; Vollmer, Beckert & Davies 2008).

There is plenty of observational evidence for the presence of nuclear star formation in AGN (Davies et al. 2007; Esquej et al. 2014) and especially in Seyfert 2s (Cid Fernandes et al. 2001; González Delgado, Heckman & Leitherer 2001). However, in the local universe, it is not clear whether there is increased star formation activity in the hosts and nuclear regions of type 2 AGN (e.g. Maiolino et al. 1995; Hicks et al. 2009) or not (Clavel et al. 2000; Peeters, Spoon & Tielens 2004), and whether the nuclear/circumnuclear star formation level is a function of the activity class (e.g. radio galaxy, quasar, infrared (IR) selected quasars; see Shi et al. 2007) and/or the AGN luminosity (Diamond-Stanic & Rieke 2012; Esquej et al. 2014). Furthermore, observational and theoretical arguments suggest the existence of dynamical delays between the onset of the nuclear star formation and the fuelling of the AGN (Davies et al. 2007; Wild, Heckman & Charlot 2010; Hopkins 2012), perhaps indicating that these two processes might not be coeval.

Classical indicators of the presence of on-going or recent star formation (e.g. UV emission, Hα, Paα, [Ne II] 12.8 µm, modelling of stellar populations) are difficult to use in the nuclear regions of AGN, as they can be easily contaminated by bright AGN emission. If we assume that polycyclic aromatic hydrocarbon (PAH) features are excited by star formation activity in AGN, they can be used as indicators of the star formation rate of galaxies based on their good correlation with the IR luminosity (Brandl et al. 2006; Smith et al. 2007). However, Peeters et al. (2004) noted that PAH emission might be better suited to trace B stars rather than O stars implying that PAH emission probes star formation over time-scales of a few tens of millions of years rather than instantaneous star formation. PAH molecules are also predicted to be excited by AGN heating at distances of approximately 100 pc from the AGN in the case of optically thin radiation (Siebenmorgen, Krügel & Spoon 2004). However, for optically thick radiation, the PAH features from star formation heating are much stronger than those due to AGN heating (see Siebenmorgen et al. 2004, for more details).

Emission from PAH features is observed in the nuclear/circumnuclear regions of AGN (Roche et al. 1991; Clavel et al. 2000; Laurent et al. 2000; Siebenmorgen et al. 2004; Deo et al. 2009; Wu et al. 2009; Diamond-Stanic & Rieke 2010, 2012; Díaz-Santos et al. 2010; Hönig et al. 2010; Sales, Pastoriza & Riffel 2010; Tommasin et al. 2010; González-Martín et al. 2013; Esquej et al. 2014). However, in general, the PAH emission in AGN appears to have a lower contrast compared to the continuum emission than in starburst galaxies. It has been argued theoretically (Voit 1992; Siebenmorgen et al. 2004) and observationally (Aiken & Roche 1985; Wu et al. 2009; Sales et al. 2010) that this might be due to destruction of the PAH molecules in the close vicinity of the harsh radiation field of AGN. However, Diamond-Stanic & Rieke (2010) showed that in local Seyferts it is only the 6.2, 7.7, and 8.6 µm PAH features that are suppressed on kpc scales with respect to the 11.3 µm PAH feature (see also Smith et al. 2007).

Recently, Esquej et al. (2014) found no evidence of destruction of the 11.3 µm PAH carriers in the nuclear regions (typically the central 60 pc) of a sample of 29 local Seyferts as a function of the AGN luminosity. These authors argued that it is likely that the PAH

molecules are protected from the AGN radiation field by material in the dusty torus (see also Voit 1992; Miles, Houck & Hayward 1994). Sales et al. (2013) came to a similar conclusion for the low-luminosity AGN in NGC 1808. Ruschel-Dutra et al. (2014), on the other hand, interpreted the non-detection of the nuclear 11.3 µm PAH feature in two Seyfert nuclei as due to destruction of the PAH molecules by the AGN radiation field.

The main goal of this work is to explore the behaviour of the 11.3 µm PAH feature and in particular whether the molecules responsible for this feature are destroyed in the close vicinity of an AGN. To this end, we have obtained mid-infrared (mid-IR) imaging and spectroscopy using CanariCam (Telesco et al. 2003) on the 10.4 m Gran Telescopio CANARIAS (GTC) of a sample of local AGN with nuclear star formation. The paper is organized as follows. Section 2 summarizes the AGN and star formation properties of the galaxies. Section 3 presents the GTC/CanariCam observations and data reduction as well as mid-IR spectroscopy obtained with the IR spectrograph (IRS; Houck et al. 2004) on board the *Spitzer Space Telescope* and Section 4 the analysis of the data. Section 5 describes the results on the extended continuum and 11.3 µm PAH feature. In Section 6, we discuss the equivalent width (EW) of the 11.3 µm feature, the nuclear spectra of Seyfert galaxies, and PAH survival in the close vicinity of AGN. Finally, we give our conclusions in Section 7. Throughout this work, we have assumed $H_0 = 73 \, \mathrm{km \, s^{-1} \, Mpc^{-1}}$, $\Omega_\Lambda = 0.73$, and $\Omega_M = 0.27$.

2 THE SAMPLE

We are conducting a mid-IR imaging and spectroscopic survey of approximately 100 local active galaxies using GTC/CanariCam. The sample includes high-luminosity AGN [Palomar-Green (PG) quasars], Seyfert galaxies, radio galaxies, and low-luminosity AGN. Some of these are hosted by luminous and ultraluminous IR galaxies (LIRGs and ULIRGs) with IR luminosities of $L_{IR} = 10^{11}-10^{12} \, L_\odot$ and $L_{IR} > 10^{12} \, L_\odot$, respectively. The sample covers almost six orders of magnitude in AGN luminosity. The GTC/CanariCam observations include imaging at 8.7 µm and 7.5−13 µm spectroscopy as well as polarimetry for selected objects.

Among the galaxies in our sample already observed with CanariCam (see Section 3.1), we selected for this work six systems for which there is evidence in the literature of AGN activity as well as nuclear and circumnuclear star formation. Additionally, we chose galaxies showing extended 11.3 µm PAH emission in the CanariCam spectra so we could investigate the effects of the AGN on the behaviour of the feature in the vicinity of the active nucleus. We list the main properties of the six systems chosen for this work in Table 1. We use, when possible, the intrinsic hard-X-ray 2–10 keV luminosity as a proxy for the AGN luminosity. In what follows, we summarize evidence of nuclear and circumnuclear on-going or recent star formation and the AGN properties for each of them. For Arp 299 (IC 694 + NGC 3690), we refer the reader to Alonso-Herrero et al. (2013b, and references therein).

Mrk 1066 (UGC 2456) – This nearly LIRG ($L_{IR} \sim 8 \times 10^{10} \, L_\odot$) is optically classified as a Seyfert 2 galaxy with star formation activity in the nuclear region on scales of ∼1.5 arcsec = 340 pc (Cid Fernandes et al. 2001; González Delgado et al. 2001; Ramos Almeida et al. 2009a; Riffel et al. 2010). In particular, Riffel et al. (2010) used near-IR integral field unit (IFU) observations to reveal the presence of two star-forming knots at projected distances of 0.5 arcsec south-east and 1 arcsec north-west from the nucleus, respectively. However, at radial distances from the AGN of less than approximately 0.5 arcsec, the near-IR line ratios are dominated by

Table 1. Properties of the GTC/CanariCam sample.

Galaxy	Optical class	b/a	z	D_L (Mpc)	Scale (pc arcsec^{-1})	IRAS $f_{12\,\mu m}$ (mJy)	log L_{IR} (L$_\odot$)	$L_{2-10\,keV}$ (erg s^{-1})	X-ray	Ref
Mrk 1066	Sy2	0.6	0.012 025	47	224	460	10.91	7.8×10^{42}	Corr	1
Mrk 1073	Sy2*	0.9	0.023 343	95	442	440	11.39	1.5×10^{41}	Obs	2
NGC 2273	Sy2	0.8	0.006 138	26	124	440	10.15	1.9×10^{42}	Corr	3
Arp 299	Sy2/L	0.9	0.010 300	44	213	3970	11.83	$1.9 \times 10^{43**}$	Corr	4
NGC 6240	L	0.5	0.024 480	103	475	590	11.85	$3.0 \times 10^{41\S}$ (N)	Obs	5
								$1.0 \times 10^{42\S}$ (S)	Obs	5
IRAS 17208−0014	L	0.8	0.042 810	181	809	200	12.41	9.3×10^{42}	Corr	6

Notes. Optical classifications are Sy = Seyfert and L = LINER. Redshifts, axis ratios b/a, luminosity distances, and projected 1 arcsec scales in parsec are from NED. The *IRAS* 12 μm flux densities and IR (8–1000 μm) luminosities are from Sanders et al. (2003). The latter are corrected to the distances used in this work. The X-ray column indicates whether the hard-X-ray luminosities are observed (Obs) or corrected (Corr) for intrinsic absorption, as listed in their corresponding references: (1) Marinucci et al. (2012); (2) Guainazzi et al. (2005); (3) Awaki et al. (2009); (4) Della Ceca et al. (2002), **the luminosity is in the 0.5–100 keV range; (5) Komossa et al. (2003), §the luminosities are in the 0.1–10 keV range; (6) González-Martín et al. (2009).
*Detection of a broad component of Paβ (Veilleux, Goodrich & Hill 1997).

AGN processes. This galaxy also shows a nuclear molecular gas disc detected in the 2.12 μm H$_2$ emission line. This gas disc is believed to provide the material to feed the AGN (Riffel & Storchi-Bergmann 2011). Mrk 1066 hosts a nearly Compton-thick Seyfert 2 nucleus (X-ray column density of $N_H = 9 \times 10^{23}$ cm^{-2}; Guainazzi, Matt & Perola 2005) with a large observed EW of the Fe Kα line at 6.4 keV. Marinucci et al. (2012) estimated an absorption-corrected intrinsic 2−10 keV luminosity of 7.8×10^{42} erg s^{-1}.

Mrk 1073 (UGC 2608) – This LIRG is located in the Perseus cluster and it is optically classified as a Seyfert 2, although it shows a broad component detected in the near-IR Paβ line (Veilleux et al. 1997). Mrk 1073 was also included in a radio-selected sample of starburst galaxies (Smith et al. 1996). Using optical spectroscopy, González Delgado et al. (2001) and Cid Fernandes et al. (2001) demonstrated that this galaxy experienced starburst activity in the central ∼1.5 arcsec = 660 pc. Mrk 1073 is a Compton-thick ($N_H > 1.6 \times 10^{24}$ cm^{-2} Guainazzi et al. 2005) Seyfert 2 with a large observed EW of the Fe Kα line. We followed Marinucci et al. (2012) to correct the observed 2–10 keV luminosity (see Table 1) and estimated an intrinsic 2–10 keV luminosity of ∼1×10^{43} erg s^{-1}.

NGC 2273 – This Seyfert 2 galaxy hosts a circumnuclear ring of star formation clearly detected in Hα+[N II] line emission with an approximate diameter of ∼4 arcsec (i.e. 500 pc), while the nuclear optical line ratios are more compatible with AGN emission (Ferruit, Wilson & Mulchaey 2000). From optical Gemini/GMOS IFU spectroscopy, there is also evidence of the presence of a nuclear ring of star formation about 2–3 arcsec in diameter, based on the presence of a nuclear velocity dispersion drop (Barbosa et al. 2006). This galaxy shows nuclear dense gas emission but based on the derived Toomre parameter, Sani et al. (2012) concluded that star formation is unlikely to be taking place in the nuclear region. Using *Suzaku* observations, Awaki et al. (2009) confirmed the Compton-thick nature of this Seyfert galaxy and derived an absorption-corrected 2−10 keV luminosity of 1.9×10^{42} erg s^{-1} (for our assumed distance).

NGC 6240 – This interacting nearly ULIRG hosts two X-ray-identified AGN at a projected separation of approximately 1.5 arcsec = 715 pc (Komossa et al. 2003). From a detailed modelling of the adaptive optics near-IR VLT/SINFONI IFU observations, Engel et al. (2010) concluded that there is recent merger-induced star formation activity in both nuclei. However, the young starbursts do not dominate the near-IR luminosity of the system. Using Keck mid-IR spectroscopy, Egami et al. (2006) showed that

the 11.3 μm PAH emission in the nuclear regions is extended over ∼3 arcsec = 1.4 kpc. The *Chandra* X-ray observations of the nuclei revealed the presence of Fe Kα lines with high EW indicating the Compton-thick nature of the nuclei. The observed 0.1−10 keV luminosities of the southern and northern nuclei are approximately 10^{42} and 3×10^{41} erg s^{-1} (Komossa et al. 2003). The absorption-corrected 2–10 keV X-ray luminosities are therefore expected to be a few times 10^{43} erg s^{-1}. By modelling the IR emission of the southern nucleus using clumpy torus models, Mori et al. (2014) estimated that the AGNs contribute to 30–50 per cent of the total luminosity of the system.

IRAS 17208−0014 – This is a late-stage merger ULIRG with a single nucleus. Arribas & Colina (2003) compared optical IFU observations with *Hubble Space Telescope* (*HST*) near-IR data and concluded that the optical peak does not coincide with the true near-IR nucleus. They also reclassified the nuclear activity to LINER. There is evidence of nuclear (∼250 pc) and extended star formation from Keck mid-IR imaging (Soifer et al. 2000). Piqueras-López et al. (2012) obtained VLT/SINFONI near-IR IFU observations of IRAS 17208−0014 and found extended Paα emission over 4 arcsec = 3.2 kpc with an off-nuclear region with a large EW of Paα and located approximately 1 kpc to the south-east. The hard-X-ray emission of this galaxy is explained by the presence of a Compton-thick AGN with an intrinsic 2–10 keV luminosity of 9×10^{42} erg s^{-1} (González-Martín et al. 2009).

Summarizing, the six systems selected for this work, even those optically classified as LINER (see Table 1), show AGN luminosities that are typical of the Seyfert galaxies in our CanariCam sample. In terms of their IR luminosities, all except NGC 2273, are nearly LIRGs, LIRGs, or ULIRGs. This is well understood because we chose them to have strong nuclear and circumnuclear star formation activity as most (U)LIRGs, and in this sense they may not be representative of the entire AGN sample. We will present a full study of the nuclear star formation activity in our sample of AGN using the 11.3 μm PAH feature once the CanariCam observations are finalized.

3 OBSERVATIONS AND DATA REDUCTION

3.1 GTC/CanariCam observations

The new CanariCam observations in this work were taken as part of an ESO/GTC large programme (182.B-2005), which totals 180 h

of observing time. At the time of writing this paper, approximately 75 per cent of the observations have already been taken. We have an additional ∼100 h for this project through the CanariCam guaranteed time programme.

We obtained imaging observations of the galaxies using the Si-2 filter ($\lambda_c = 8.7$ μm and width $\Delta\lambda_{cut} = 1.1$ μm at 50 per cent cut-on/off). The observations were taken in queue mode under photometric conditions using the standard mid-IR chop-nod technique. The chop and nod throws were 15 arcsec, whereas the chop and nod angles were chosen for each target to avoid extended galaxy emission in the sky image. We also observed standard stars immediately before or after the galaxy observations to perform the photometric calibration, measure the image quality (IQ) of the observations, and perform the point spread function (PSF) subtraction.

The plate scale of the CanariCam 320 × 240 Si:As detector is 0.0798 arcsec pixel^{-1}, which provides a field of view in imaging mode of ∼26 arcsec × 19 arcsec. We measured the IQ of the data by fitting the observations of the standard stars with a Gaussian function and obtained values of 0.2–0.4 arcsec (full width half-maximum, FWHM). In Table 2, we summarize details of the imaging observations, including the date of the observations, the on-source integration time t_{on}, the standard star used, and the IQ of the observations.

We also obtained long-slit spectroscopy of the nuclear regions of the galaxies using the low-spectral-resolution 10 μm grating, which covers the *N* band ∼7.5–13 μm with a nominal spectral resolution of $R = \lambda/\Delta\lambda \sim 175$. We used a 0.52 arcsec wide slit for all the galaxies with the position angles (PA) of the slits, measured from north to east, listed in Table 3. The observing sequence was first to take an acquisition image of the galaxy with the Si-2 filter, then place the slit, and finally integrate for the on-source times given in Table 3. The chop-nod parameters were as for the imaging observations. We also observed standard stars using the same observing sequence to provide the photometric calibration, the telluric correction, and the slit loss correction. We also used the acquisition images of the standard stars to obtain the IQ of the observations (see Table 3).

We reduced the data using the CanariCam pipeline REDCAN, which is thoroughly described by González-Martín et al. (2013). Briefly, the reduction process of the imaging data includes sky subtraction, stacking of the individual images, and rejection of bad images. The

Table 2. Log of the GTC/CanariCam imaging observations.

Galaxy	Date	t_{on} (s)	Standard	IQ (arcsec)
Mrk 1066	2013-08-27	417	HD18449	0.24
Mrk 1073	2013-08-27	626	HD19476	0.26
NGC 2273	2013-09-24	626	HD42633	0.26
NGC 6240	2013-08-27	626	HD151217	0.38
IRAS 17208−0014	2013-06-07	1043	HD157999	0.26

Table 3. Log of the GTC/CanariCam spectroscopic observations.

Galaxy	Date	t_{on} (s)	PA (°)	Standard	IQ (arcsec)
Mrk 1066	2013-08-31	1061	315	HD18449	0.28
Mrk 1073	2013-09-10	1238	75	HD14146	0.34
NGC 2273	2013-09-23	884	290	HD42633	0.26
	2013-09-22	354	290	HD42633	0.32
NGC 6240	2013-09-15	1238	16	HD157999	0.40
IRAS 17208−0014	2013-09-09	1238	90	HD157999	0.30

flux calibration of the galaxy images is done using the observations of the standard stars. We show the fully reduced GTC/CanariCam 8.7 μm images of the galaxies of our sample in the top panels of Figs 1–5.

For the spectroscopy, the first three steps of the data reduction are the same as for the imaging. Additionally, REDCAN performs the two-dimensional (2D) wavelength calibration of the galaxy and standard star spectra using sky lines. Finally, the trace determination is done using the standard star data. Figs 1–5 (middle panels) show 2D spectral images after the wavelength calibration but before correction for atmospheric transmission. From these figures, we can clearly observe nuclear and extended emission of the 11.3 μm PAH feature in all five galaxies. The last steps of the spectroscopic data reduction are the spectral extraction either as point sources or extended sources (see Section 4.2), and finally, the correction for slit losses in the case of point source extractions.

3.2 *Spitzer*/IRS spectroscopy

All the galaxies in our sample were observed with *Spitzer*/IRS using the short-low (SL) spectral resolution ($R \sim 60$–120) module covering the spectral range ∼5–15 μm. Table 4 summarizes information about the observations. All the observations were taken in staring mode, except for those of Arp 299 which were taken using the IRS spectral mapping mode capability. Alonso-Herrero et al. (2009) and Alonso-Herrero et al. (2013b) provide all the details on the data reduction and extraction of the nuclear spectra of Arp 299 as a point source, respectively. For the rest of the galaxies observed in staring mode, we downloaded the fully calibrated spectra from the Cornell Atlas of *Spitzer*/IRS Sources (CASSIS v4; Lebouteiller et al. 2011). CASSIS provides spectra with optimal extraction regions to ensure the best signal-to-noise (S/N) ratio. For the galaxies in this work, the optimal CASSIS extraction was equivalent to a point source extraction. The SL slit width of these observations is 3.7 arcsec.

4 ANALYSIS

4.1 Imaging: source size and aperture photometry

We measured the size of the nuclear regions before rotating and smoothing the GTC/CanariCam images using a Gaussian function. The measured sizes (FWHM) of the mid-IR emission in arcseconds and pc for the nuclear regions of the galaxies are listed in Table 5. The nuclear sizes (0.3–0.4 arcsec) at 8.7 μm of Mrk 1066, Mrk 1073, NGC 2273, and NGC 6240S are consistent with the presence of an unresolved source, although there is also extended emission. The nuclear region of IRAS 17208−0014 and NGC 6240N appear clearly resolved at 8.7 μm, in good agreement with previous observations for instance at near-IR wavelengths (see e.g. Engel et al. 2010; Piqueras-López et al. 2012, respectively).

We performed aperture photometry on the images using IRAF[1] routines. The nuclear 8.7 μm flux densities (without the correction for point source emission) measured through different apertures are given in Table 5. We also list in this table the uncertainties due to the background subtraction, which increase with the size of the aperture used. Additionally, the typical errors of the photometric

---

[1] IRAF is distributed by the National Optical Astronomy Observatory, which is operated by the Association of Universities for Research in Astronomy (AURA) under cooperative agreement with the National Science Foundation.
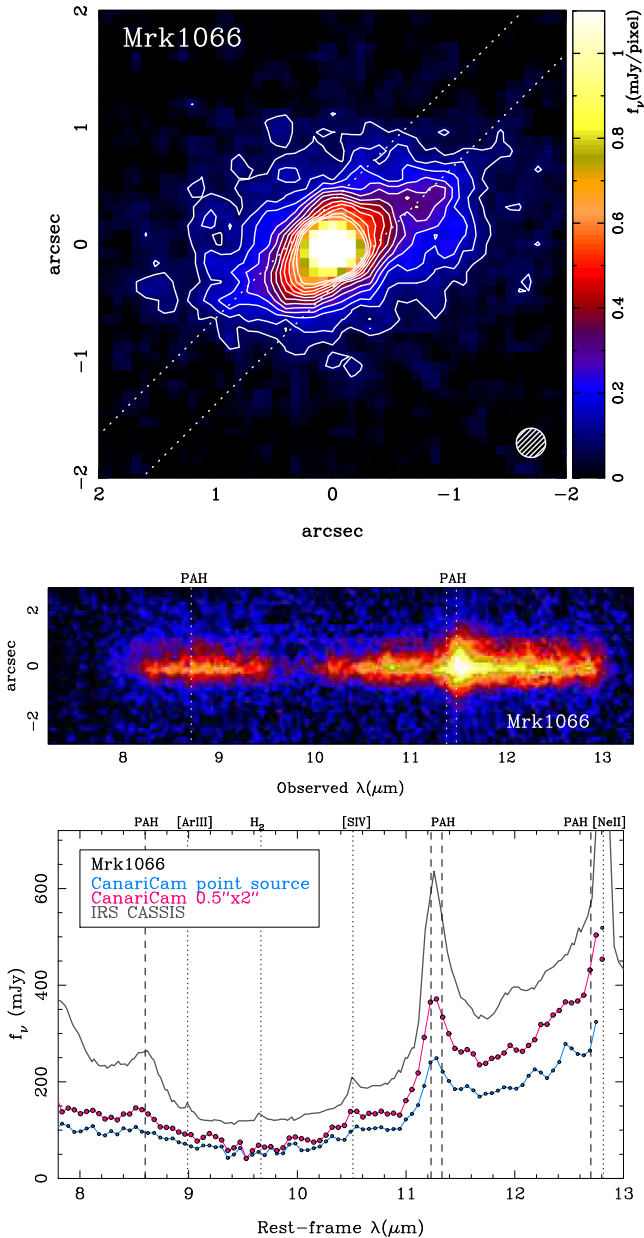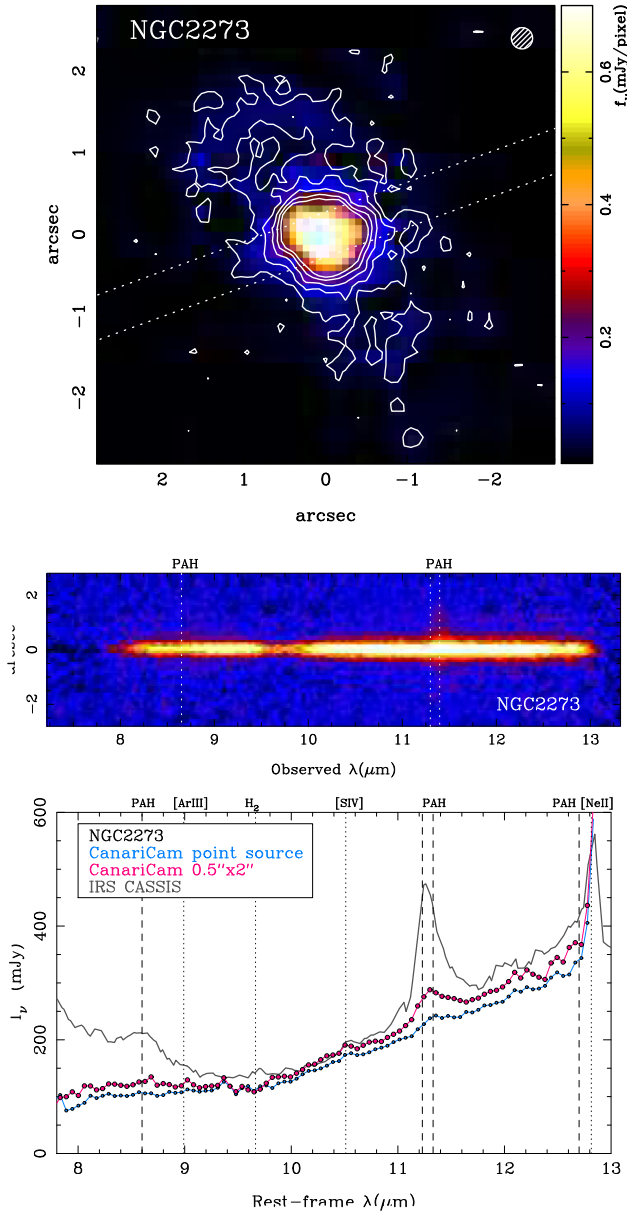
Figure 1. Mrk 1066. The top panel is the GTC/CanariCam Si-2 ($\lambda_c = 8.7\,\mu$m) image on a colour linear scale as plotted on the right-hand side. Orientation is north up, east to the left. The image was smoothed with a Gaussian function with $\sigma = 0.6$ pixels. The contours are also in a linear scale with the lowest contour corresponding to the local background value plus 1.5 standard deviations measured in the image before rotating and smoothing the images. The hatched circle represents the angular resolution of the image (FWHM) approximated as a Gaussian function. The dotted lines show the approximate width and orientation of the slit. The middle panel shows the partially reduced GTC/CanariCam 2D spectrum in a square-root colour scale and smoothed with a Gaussian function. On the y-axis positive offsets indicate north-west and negative offsets south-east. The bottom panel compares the GTC/CanariCam nuclear and 0.52 arcsec × 2 arcsec spectra with the *Spitzer*/IRS SL spectrum extracted as a point source. We smoothed the GTC/CanariCam spectra by averaging together three pixels in the spectral direction.
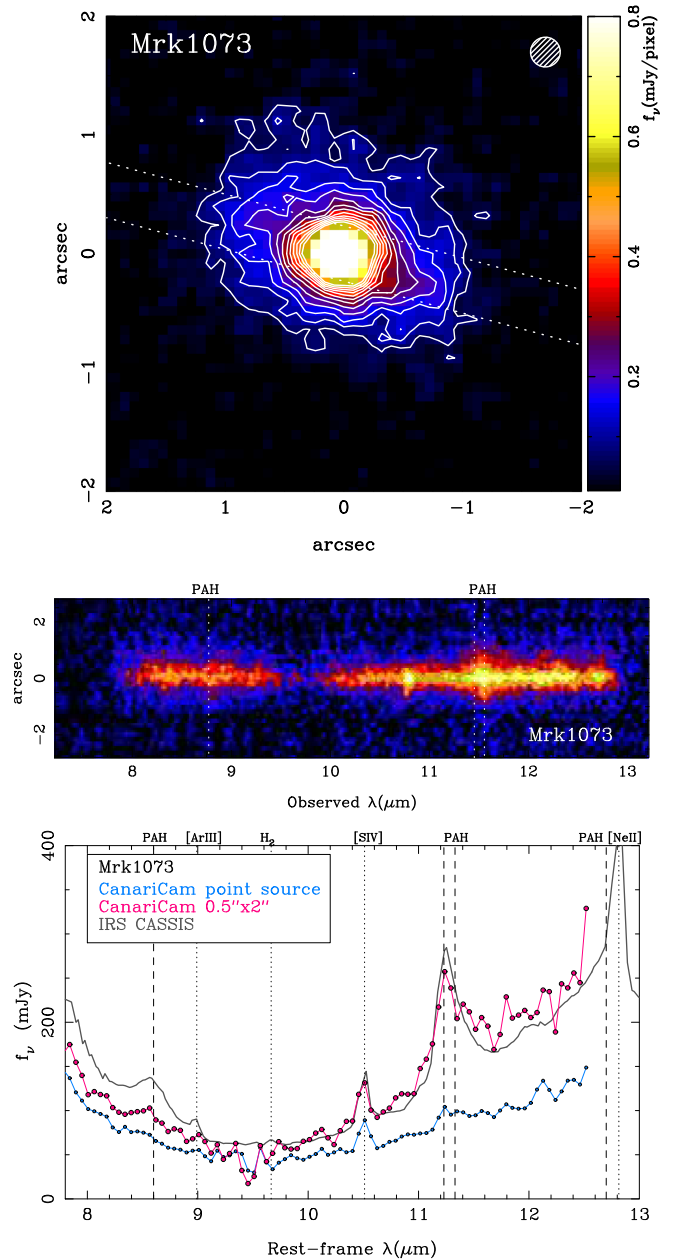
Figure 2. Mrk 1073. Symbols as in Fig. 1. The top panel is the GTC/CanariCam 8.7 μm image smoothed with a Gaussian function with $\sigma = 0.6$ pixels. The contours are in a linear scale with the lowest contour corresponding to the local background value plus two standard deviations measured in the image before rotating and smoothing the images. The middle panel is the partially reduced GTC/CanariCam 2D spectrum. On the y-axis positive offsets indicate north-east and negative offsets south-west. The bottom panel compares the 1D GTC/CanariCam spectra (smoothed as in Fig. 1, bottom panel) and the *Spitzer*/IRS spectrum. The GTC/CanariCam 0.52 arcsec × 2 arcsec spectrum of Mrk 1073 was scaled down by a factor of 1.8 to match the IRS one.

calibration in the *N*-band window are estimated to be approximately 10–15 per cent.

For those galaxies with nuclear FWHMs similar to those of their corresponding standard stars, we also estimated the unresolved nuclear fluxes. To do so, we used the fluxes measured through the smallest aperture and estimated the aperture correction for the total
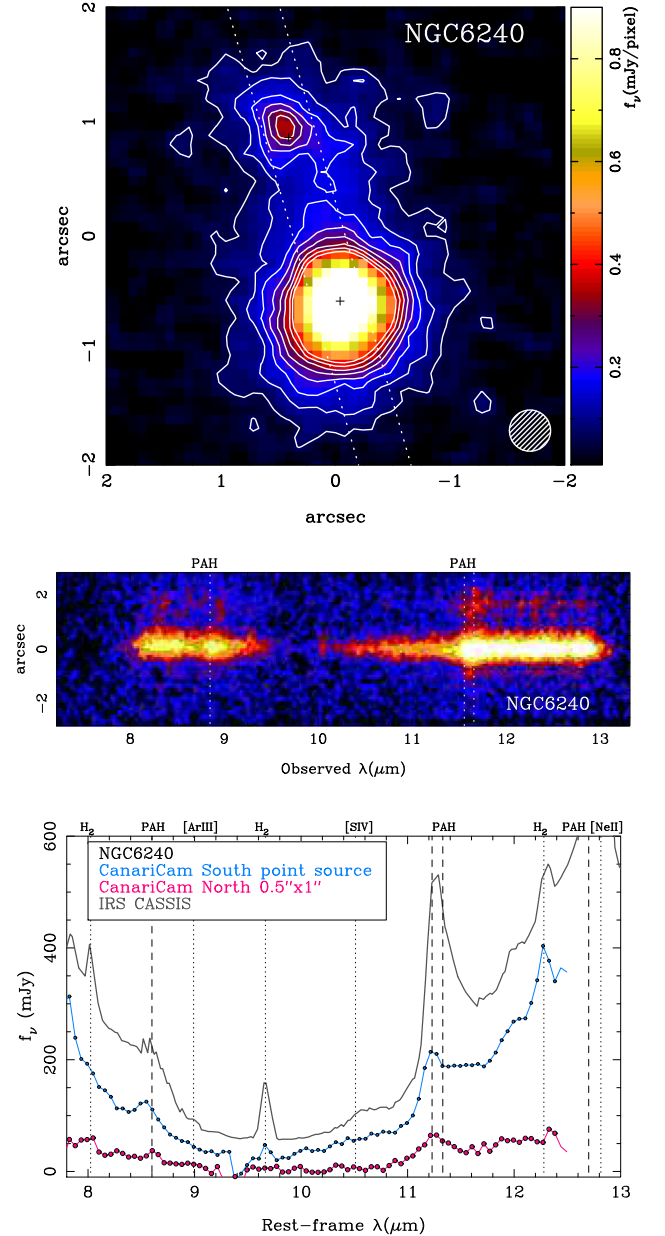
Figure 3. NGC 2273. Symbols as in Fig. 1. The top panel is the GTC/CanariCam 8.7 μm image smoothed with a Gaussian function with $\sigma = 0.7$ pixels. The contours are in a linear scale with the lowest contour corresponding to the local background value plus one standard deviation measured in the image before rotating and smoothing the images. The middle panel is the partially reduced GTC/CanariCam 2D spectrum. On the y-axis positive offsets indicate north-west and negative offsets south-east. The bottom panel compares the 1D GTC/CanariCam spectra (smoothed as in Fig. 1, bottom panel) and the *Spitzer*/IRS spectrum.

flux using the standard star observations. We note that the unresolved nuclear fluxes estimated using this method (see Table 5) are likely to be slightly overestimated as there is always a small fraction of resolved emission from the galaxy even in the smallest aperture. This is the case for Mrk 1066, where Ramos Almeida et al. (2014) estimated an unresolved nuclear flux by PSF scaling of 63 ± 9 mJy.

4.2 Extracting spectra

For all the galaxies except NGC 6240N and IRAS 17208−0014, which appear resolved in the GTC/CanariCam images at 8.7 μm

Figure 4. NGC 6240. Symbols as in Fig. 1. The top panel is the GTC/CanariCam 8.7 μm image smoothed with a Gaussian function with $\sigma = 0.7$ pixels. The contours are in a linear scale with the lowest contour corresponding to the local background value plus 1.5 standard deviations measured in the image before rotating and smoothing the images. The crosses indicate the positions of the radio sources (Beswick et al. 2001) after we made the radio southern source coincident with the bright mid-IR southern nucleus. The middle panel is the partially reduced GTC/CanariCam 2D spectrum. On the y-axis positive offsets indicate north-east and negative offsets south-west. The northern nucleus is located at approximately $+1.5$ arcsec from the southern nucleus. In the bottom panel are the 1D GTC/CanariCam spectra (smoothed as in Fig. 1, bottom panel) through extraction apertures centred on the southern and northern nuclei compared to the *Spitzer*/IRS SL spectrum, which encompasses both nuclei.

(see previous section and Table 5), we extracted the nuclear spectra as point sources. In this case, REDCAN uses an extraction aperture that increases with wavelength to take care of the decreasing angular resolution. It also performs a correction to account for slit losses. We
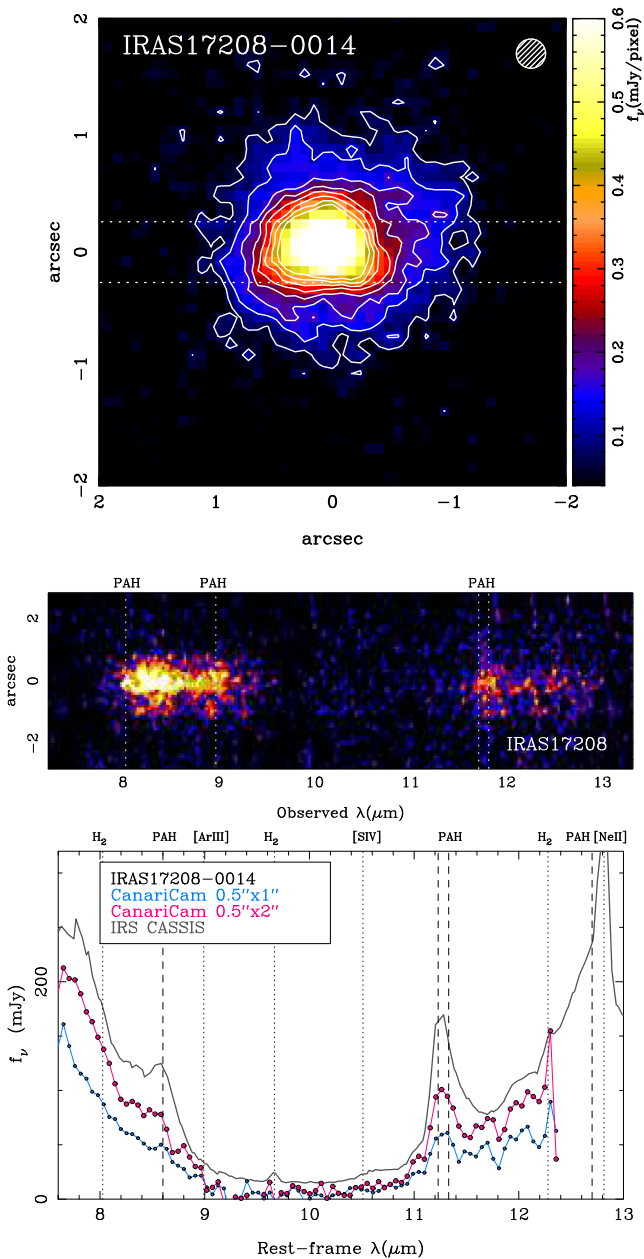
Figure 5. IRAS 17208−0014. Symbols as in Fig. 1. The top panel is the GTC/CanariCam 8.7 μm image smoothed with a Gaussian function with σ = 0.6 pixels. The contours are in a linear scale with the lowest contour corresponding to the local background value plus two standard deviations measured in the image before rotating and smoothing the images. The middle panel is the partially reduced GTC/CanariCam 2D spectrum. On the *y*-axis positive offsets indicate east and negative offsets west. The bottom panel compares the 1D GTC/CanariCam spectra (smoothed as in Fig. 1, bottom panel) and the *Spitzer*/IRS spectrum.

checked the flux calibration of the nuclear spectra against the photometry done on the GTC/CanariCam 8.7 μm images after applying a correction for point source emission. We found good agreement between them to within 15–20 per cent. We also extracted spectra for all the galaxies as extended sources using an aperture of 0.52 arcsec × 2 arcsec. For NGC 6240N and IRAS 17208−0014, we extracted the nuclear spectra as extended sources with a 0.52 arcsec × 1 arcsec extraction aperture.

In Figs 1–5 (bottom panels), we compare the GTC/CanariCam flux-calibrated nuclear and 0.52 arcsec × 2 arcsec spectra with the CASSIS *Spitzer*/IRS SL spectra. The SL IRS spectra have an approximate angular resolution of ∼4 arcsec.

The 2D GTC/CanariCam spectra of Mrk 1066, Mrk 1073, and NGC 6240 show high-S/N extended 11.3 μm PAH emission and continuum emission (see Figs 1, 2, and 4, respectively). Therefore, for these galaxies, we investigate the spatial variations of the EW and flux of the 11.3 μm PAH feature and local continuum in Section 5. To do so, we used REDCAN to extract from the wavelength-calibrated 2D images the nuclear spectra as well as spectra at different radial distances along the slit out to 1.5−2 arcsec on both sides of the nuclei by binning together four pixels (0.32 arcsec) in the spatial direction and assuming an extended source extraction.

4.3 Measuring the 11.3 μm PAH feature

For each of the extracted GTC/CanariCam and *Spitzer*/IRS spectra, we measured the flux and EW of the 11.3 μm PAH feature following the method described in Hernán-Caballero & Hatziminaoglou (2011) and implemented for ground-based spectroscopy by Esquej et al. (2014). We fitted a local continuum at 11.25 μm by interpolating between two narrow bands (10.75–11.0 μm and 11.65–11.9 μm) on both sides of the feature. To measure the flux of the PAH feature, we integrated the spectrum in the range $\lambda_{rest} = 11.05$–11.55 μm (see Hernán-Caballero & Hatziminaoglou 2011, for full details).

We estimated the uncertainties in the measurements by performing Monte Carlo simulations using the calculated dispersion around the measured fluxes and EWs in 100 simulations of the original spectrum with random noise distributed as the rms for the GTC/CanariCam data and error of the spectra for the Spitzer/IRS data. PAH fluxes obtained with a local continuum are lower than those using a continuum fitted over a large spectral range (e.g. measurements done with PAHFIT; see Smith et al. 2007). We therefore corrected the measured fluxes of the 11.3 μm PAH feature by applying a multiplicative factor of 2 as derived by Smith et al. (2007). For more details, we refer the reader to Esquej et al. (2014). We list the 11.3 μm PAH measurements in Table 6, including those of the two nuclei of Arp 299 (NGC 3690 and IC 694).

For reference, galaxies with EW(11.3 μm PAH) ≤ 0.1 μm are AGN dominated in the mid-IR, whereas those with EW(11.3 μm PAH) ≥ 0.2 μm would have a starburst contribution to the mid-IR emission greater than 50 per cent (see Hernán-Caballero & Hatziminaoglou 2011).

5 EXTENDED NUCLEAR MID-IR EMISSION

In this section, we present the results on the extended nuclear mid-IR emission as derived from the GTC/CanariCam imaging and spectroscopy and compare them with *Spitzer*/IRS SL spectroscopy, which probes larger physical scales.

5.1 Mrk 1066

The GTC/CanariCam 8.7 μm image of Mrk 1066 (Fig. 1) shows a bright unresolved nuclear source (FWHM ≤67 pc, see Table 5) as well as disc-like extended emission detected out to radial distances of approximately 1.5 arcsec. The extended component has a morphology similar to that observed in the near-IR continuum (Quillen et al. 1999) and Paβ and Brγ hydrogen recombination lines (see fig. 4 of Riffel et al. 2010). The region with extended emission contains the narrow-line region (NLR) detected in the optical [O III]λ5007

Table 4. *Spitzer*/IRS spectroscopy.

Galaxy	Programme ID	PI	Cycle	Mode
Mrk 1066	30572	V. Gorjian	6	Staring
Mrk 1073	30323	L. Armus	6	Staring
NGC 2273	86	M. Werner	1	Staring
Arp 299	21	J. R. Houck	1	Spectral mapping
NGC 6240	105	J. R. Houck	1	Staring
IRAS 17208−0014	105	J. R. Houck	1	Staring

Table 5. GTC/CanariCam aperture photometry and unresolved nuclear fluxes at 8.7 µm.

Galaxy	FWHM			Fluxes				
	Nucleus		0.48 arcsec	0.96 arcsec	1.92 arcsec	4 arcsec	Unresolved
	(arcsec)	(pc)	(mJy)	(mJy)	(mJy)	(mJy)	(mJy)
Mrk 1066	0.30	67	41 ± 1	79 ± 3	135 ± 10	193 ± 30	75
Mrk 1073	0.33	146	30 ± 1	60 ± 1	109 ± 5	160 ± 20	57
NGC 2273	0.30	37	53 ± 1	94 ± 2	132 ± 8	189 ± 30	113
NGC 6240N	0.45	214	8 ± 1	20 ± 4	–	–	–
NGC 6240S	0.38	181	45 ± 1	98 ± 4	–	231 ± 19^a	165
IRAS 17208−0014	0.52	421	23 ± 1	55 ± 1	105 ± 3	151 ± 8	–

Notes. The listed apertures are diameters. The quoted errors in the photometry are only due to uncertainties in the background estimate. [a]The 4-arcsec-diameter photometry for NGC 6240 is for an aperture centred between the two nuclei.

Table 6. Measurements of the 11.3 µm PAH feature.

Galaxy	GTC/CanariCam nuclear			*Spitzer*/IRS circumnuclear			$L_{11.3\,\mu m\,PAH}$
	Region (pc)	EW (µm)	Lum (erg s^{-1})	Region (kpc)	EW (µm)	Lum (erg s^{-1})	Nuc/Circum
Mrk 1066	$\leq$116	0.35 ± 0.02	5.6×10^{41}	0.8	0.53 ± 0.01	1.6×10^{42}	0.35
Mrk 1073	$\leq$230	0.08 ± 0.03	3.2×10^{41}	1.6	0.43 ± 0.01	2.8×10^{42}	0.11
NGC 2273	$\leq$64	0.03 ± 0.01	2.8×10^{40}	0.5	0.33 ± 0.01	3.1×10^{41}	0.09
NGC 3690	$\leq$111	$\leq$0.01	$\leq 9.3 \times 10^{40}$	0.8	0.13 ± 0.01	1.6×10^{42}	$\leq$0.06
IC 694	$\leq$111	0.14 ± 0.01	2.9×10^{41}	0.8	0.51 ± 0.01	2.5×10^{42}	0.12
NGC 6240N	247×475	0.86 ± 0.11	1.4×10^{42}	1.8	0.62 ± 0.01^a	$7.1 \times 10^{42*}$	0.20
NGC 6240S	$\leq$247	0.27 ± 0.01	2.0×10^{42}				0.28
IRAS 17208−0014	421×809	0.56 ± 0.08	2.4×10^{42}	3.0	0.90 ± 0.01	7.8×10^{42}	0.31

Notes. For the nuclei not resolved by CanariCam, the quoted size (diameter) of the region is less or equal to the slit width. For the *Spitzer*/IRS SL data, the size of the region is the slit width. We applied a multiplicative factor of 2 to the measured 11.3 µm PAH luminosities to be able to compare with results obtained with PAHFIT. See Section 4.3 for details.
[a]The *Spitzer*/IRS SL spectroscopy of NGC 6240 includes the two nuclei of the system (Armus et al. 2006).

emission line and also regions with active star formation (see Riffel et al. 2010, and references therein). The similarity between the extended 8.7 µm emission[2] and hydrogen recombination lines is common in other IR bright galaxies and star-forming galaxies (Helou et al. 2004; Alonso-Herrero et al. 2006; Díaz-Santos et al. 2008). This in principle suggests that the mid-IR extended emission at 8 µm traces sites of on-going or recent star formation activity but there can be some contribution from dust in the NLR in AGN (see e.g. Radomski et al. 2003; Packham et al. 2005).

For the GTC/CanariCam spectroscopy, we oriented the slit along the major axis of the extended mid-IR emission at a PA =315°. In Fig. 1, we compare the nuclear and 0.52 arcsec × 2 arcsec GTC/CanariCam spectra with the *Spitzer*/IRS spectrum. The nu-

clear spectrum probes approximately a region of 116 pc in size[3] and shows bright 11.3 µm PAH emission (also from the 8.6 µm PAH feature). This is indicative of the presence of nuclear star formation activity. There is also evidence of the silicate feature in absorption. The nuclear contribution to the ∼4 arcsec (∼0.9 kpc) 11.3 µm PAH feature measured in the *Spitzer*/IRS spectrum is 35 per cent (see Table 6). Based on the EW of the 11.3 µm PAH feature in the *Spitzer*/IRS spectrum, Hernán-Caballero & Hatziminaoglou (2011) classified this galaxy as starburst, while the nuclear value of the EW is lower, as expected, due to the higher contribution from the AGN continuum (see discussion in Section 6.1, and also Ramos Almeida et al. 2014).

We can make use of the spatial information afforded by the GTC/CanariCam spectroscopy to produce spatial profiles of the

---

[2] The GTC/CanariCam Si-2 filter includes contributions from both the 8.6 µm PAH feature and the underlying continuum, as can be seen from fig. 4 in Díaz-Santos et al. (2008).

[3] Since this galaxy is inclined at ∼50°, the region encompassed by the slit is larger than that indicated by the projected slit width.
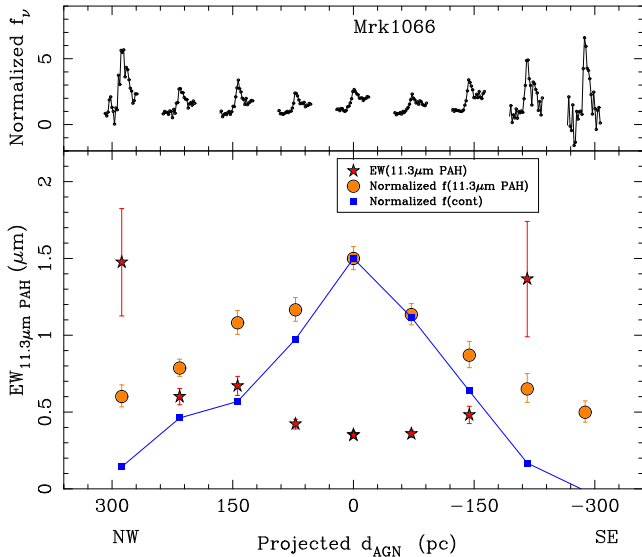
Figure 6. Lower panel: GTC/CanariCam spatial profiles of Mrk 1066 as a function of the projected distance from the AGN d_{AGN}. We show the profiles of the EW and flux of the 11.3 μm PAH feature as star-like symbols and filled dots, respectively, and the flux of the local continuum at 11.25 μm as filled squares. The measured fluxes are normalized to the peak intensity at the nuclear position, which is set at the 0 position on the *x*-axis, and set to a 1.5 value on the *y*-axis. For clarity, we plotted only the errors in the measured EW and flux of the PAH feature. Top panel: spectra around the 11.3 μm PAH feature ($\lambda_{rest} = 10.5$–12 μm), normalized to the same continuum level at ∼10.9 μm for the spatial location of each of the extracted spectra.

mid-IR emission (Section 4.2). Fig. 6 shows the spatial profiles of the EW of the 11.3 μm PAH feature (star symbols) and its normalized flux (circles) together with the normalized local continuum (squares) as a function of the projected distance from the AGN, d_{AGN}. The 11.3 μm PAH emission is detected out to projected radial distances of ∼300 pc on both sides of the nucleus. The intensity of the PAH feature peaks at the nucleus. From the modelling of the optical spectrum, González Delgado et al. (2001) showed that the nuclear emission of Mrk 1066 is dominated by the emission of young and intermediate-age stellar populations. Since we detected nuclear 11.3 μm PAH emission in the central ∼100 pc and PAH molecules are excited by the UV emission from O stars and B stars (Peeters et al. 2004), we conclude that the 11.3 μm PAH emission can be used to reveal the presence of on-going/recent nuclear star formation in the nuclear regions of AGN.

The spatial profile of the local interpolated continuum at 11.25 μm measured from the GTC/CanariCam spectrum has its maximum also at the nucleus, but it is narrower than that of the PAH feature. This indicates that in the nuclear region the continuum at this wavelength has a strong component presumably arising from the unresolved AGN emission. Additionally, the PAH spatial profile shows a secondary peak at a radial distance of ∼150 pc to the north-west that is approximately coincident with one of the starburst sites detected in the near-IR (see Riffel et al. 2010). Also, on both sides of the nucleus the PAH flux profile extends out to the radial distances of ∼300 pc.

The spatial profile of the EW of the 11.3 μm PAH feature shows a minimum (EW = 0.35 ± 0.02 μm) at the nuclear position, which is typical of Seyfert galaxies with nuclear/circumnuclear star formation (Sales et al. 2010; Tommasin et al. 2010; Hernán-Caballero & Hatziminaoglou 2011; Esquej et al. 2014). At larger radial distances from the nucleus, the EW of the feature increases reaching values
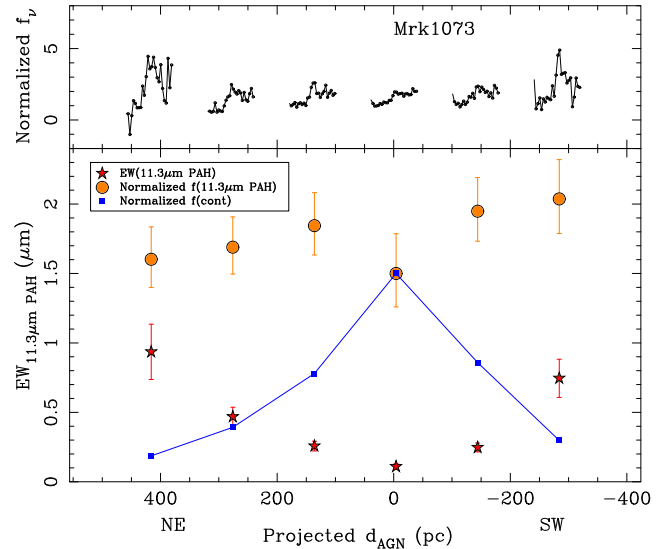
**Figure 7.** As Fig. 6, but for Mrk 1073.

typical of star-forming galaxies (EW ∼ 0.5–1 μm). This behaviour is well understood in terms of the increased continuum from the AGN towards the nuclear regions rather than a fall-off of the PAH emission because the 11.3 μm PAH feature peaks at the nucleus (see a detailed discussion in Section 6.1). Even at the location of the two starburst sites, the observed EW of the feature still has a relatively low value due to contamination from continuum produced by AGN-heated dust. Indeed, when the extracted spectra are corrected for this AGN contamination, the measured EW are consistent with pure star formation. We refer the reader to Ramos Almeida et al. (2014) for a detailed study of the star formation and torus properties of this galaxy.

5.2 Mrk 1073

The GTC/CanariCam 8.7 μm image (Fig. 2) shows a bright unresolved nuclear source with an FWHM size of ≤146 pc (see Table 5). There is also extended emission in the disc of the galaxy with an approximate diameter of 2.6 arcsec ≃ 1.1 kpc. For the spectroscopy, we placed the GTC/CanariCam slit along the major axis of this emission (PA = 75°).

The GTC/CanariCam nuclear spectrum of Mrk 1073 shows the silicate feature in moderate absorption with weak 8.6 and 11.3 μm PAH emission (Fig. 2, bottom panel). The PAH features become more apparent on the ∼1.6 kpc scale probed by the *Spitzer*/IRS spectrum with an EW of the 11.3 μm PAH feature being consistent with a composite AGN/starburst nature (Sales et al. 2010; Tommasin et al. 2010; Hernán-Caballero & Hatziminaoglou 2011; Esquej et al. 2014). The nuclear contribution to the observed 11.3 μm PAH feature luminosity in the central 1.6 kpc of Mrk 1073 is only 11 per cent, but consistent with findings for other Seyfert galaxies (see Esquej et al. 2014). The low value of the nuclear EW of the 11.3 μm PAH feature (EW = 0.08 ± 0.03 μm, see Table 6) clearly indicates that on nuclear scales the mid-IR emission of Mrk 1073 is dominated by emission from the AGN, unless the PAHs get destroyed by the AGN (but see Section 6.3).

Fig. 7 shows the spatial profiles of the flux and EW of the 11.3 μm PAH feature emission and the flux of the local continuum at 11.25 μm. The PAH feature is detected out to projected distances from the AGN of ∼400 and ∼300 pc to the north-east
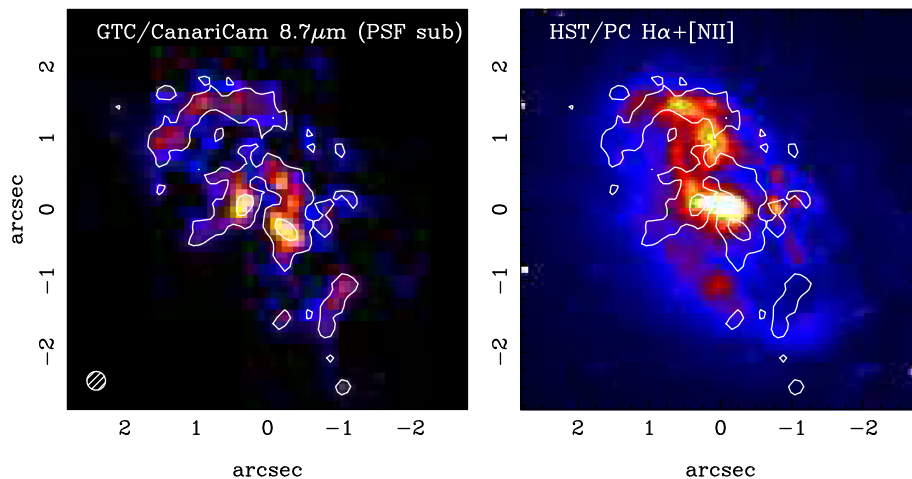
Figure 8. NGC 2273. Left-hand panel: GTC/CanariCam PSF-subtracted 8.7 μm in a square-root colour scale. The hatched circle is the FWHM of the PSF. Right-hand panel: *HST*/PC Hα+[N II]+continuum image with the 8.7 μm contours superimposed. The lowest 8.7 μm contour is as in Fig. 3 (top panel).

and south-west of the nucleus, respectively. This confirms that the extended 8.7 μm emission detected in the GTC/CanariCam image is due to star formation activity. Unlike Mrk 1066, the PAH feature emission does not peak strongly at the nucleus, but rather it is approximately uniform along the spatial direction at PA =75°. This is in good agreement with the relatively constant contribution of the young stellar populations (≤100 Myr) in the central few kpc of this galaxy (Raimann et al. 2003). We note that the spatial profiles plot the observed (not corrected for extinction) flux of the 11.3 μm PAH feature. The slight decrease of the flux of the PAH feature at the location of the nucleus might be due to a higher extinction there as indicated by the moderate depth of the silicate feature. The EW of the 11.3 μm, on the other hand, has its minimum value in the nuclear region, consistent with the presence of a strong AGN-produced continuum there. At projected distances, ∼300 pc and further away from the nucleus, the measured values of the EW are consistent with that observed in regions of pure star formation activity.

5.3 NGC 2273

The GTC/CanariCam 8.7 μm image of NGC 2273 (see Fig. 3) shows a bright nuclear point source with an unresolved size of ≤37 pc (FWHM). There is also diffuse emission out to a radial distance of approximately 1.5 arcsec = 190 pc, which appears to be more prominent to the north of the nucleus.

Ferruit et al. (2000) detected a ring of star formation using *HST* narrow-band Hα+[N II] imaging. To compare the extended mid-IR and optical emission, we first subtracted the bright nuclear unresolved component in the GTC/CanariCam images. We used the standard star observation taken for the photometric calibration as a representation of the PSF and followed the method for PSF subtraction explained by Ramos Almeida et al. (2009b). We note that we did the PSF subtraction before rotating and smoothing the NGC 2273 image. We used the bright nuclear emission to align the optical and mid-IR images.

Fig. 8 shows the PSF-subtracted 8.7 μm image compared with the Hα+[N II] image. The diffuse emission detected at 8.7 μm to the north of the nucleus at ∼1.5 arcsec has a reasonable resemblance with the optical line emission. Some of the differences might be due to the fact that we did not subtract the continuum from the optical line image. Therefore, there is an additional component due to stellar emission. To the south of the nucleus, the emission from the

ring appears less prominent. In the central 2 arcsec = 250 pc, the PSF-subtracted 8.7 μm image reveals the presence of extended nuclear emission[4] with a similar orientation as the Hα+[N II] nuclear emission. Since there is also diffuse extended 11.3 μm PAH emission in the nuclear region, as can be seen from the 2D GTC/CanariCam spectrum (Fig. 3), the extended emission in the Si-2 filter has likely a contribution from the 8.6 μm PAH feature. This extended nuclear emission might be related to dense molecular gas emission detected in the nuclear region (central ∼2 arcsec) of this galaxy (see Sani et al. 2012) and the nuclear ring identified by Barbosa et al. (2006) by the presence of a velocity dispersion (σ) drop. The nuclear *HST* optical line ratios appear to have some contribution from the NLR emission (Ferruit et al. 2000).

The GTC/CanariCam nuclear spectrum of NGC 2273 (see Fig. 3) is dominated by the bright AGN continuum with weak, but detectable, 11.3 μm PAH emission with EW = 0.03 ± 0.01 μm. The modest angular resolution and high sensitivity of the *Spitzer*/IRS SL spectrum, on the other hand, capture the diffuse emission within the central 4 arcsec ∼ 500 pc as bright 8.6 and 11.3 μm PAH emission. The measured EW of the 11.3 μm PAH feature within the IRS aperture reflects the starburst/AGN composite nature of the emission (see Sales et al. 2010; Tommasin et al. 2010; Hernán-Caballero & Hatziminaoglou 2011; Esquej et al. 2014).

The nuclear contribution to the observed 11.3 μm PAH emission within this region is 9 per cent, thus indicating that most of the star formation in the central 500 pc of this galaxy arises from the circumnuclear ring (that is, outside the inner ∼60 pc). Still, the detection of the 11.3 μm PAH feature in the nuclear region (inner ≤64 pc) implies a star formation rate of 0.08 M$_\odot$ yr^{-1} (0.21 M$_\odot$ yr^{-1} for the ∼60 pc × 250 pc aperture), using the calibration of Diamond-Stanic & Rieke (2012). This appears in contradiction with the Toomre parameter calculated by Sani et al. (2012) that seems to indicate that the central ∼100 pc of this galaxy should be stable against star formation.

5.4 Arp 299

The GTC/CanariCam observations and modelling of the AGN properties of this interacting system were presented in Alonso-Herrero

---

[4] We note that some of the structure seen there, especially the two knots at PA of about 50°, might be due to imperfect PSF subtraction.

et al. (2013b). Here, we only discuss briefly the 11.3 µm PAH feature. In the nuclear region of the eastern component of Arp 299, IC 694, the nuclear 11.3 µm PAH feature is detected with EW = 0.14 ± 0.01 µm, which is indicative of a composite starburst/AGN nature. Alonso-Herrero et al. (2000) concluded that the IR emission of this component is dominated by star formation activity. However, there is also evidence of the presence of AGN activity, based on the reduced EW when compared to that measured on kpc scales with *Spitzer*/IRS and the modelling of the nuclear spectrum (Alonso-Herrero et al. 2013b).

In the case of NGC 3690, the nucleus of the western component of Arp 299, the nuclear (distance from the AGN $d_{AGN} \leq 50$ pc) 11.3 µm PAH feature is not detected. The 2σ upper limit is EW ≤ 0.01 µm, whereas in the IRS spectrum, we measured EW = 0.13 ± 0.01 µm. Alonso-Herrero et al. (2000) showed that the star formation rate in the nucleus of NGC 3690 is about five time less than in IC 694. The upper limit (at the 2σ level) to the 11.3 µm PAH luminosity in the nucleus of NGC 3690 compared with that of IC 694 (see Table 6) is compatible with this. We cannot therefore reach a firm conclusion as to whether PAHs are destroyed near the nucleus of NGC 3690 or the low EW is due to dilution by the luminous AGN continuum (Section 6.1). We also note that the *HST*/NICMOS Paα image shows that there is extended emission approximately 1.1 arcsec south-west from the nucleus of NGC 3690 (i.e. sources B16 and B1, respectively, see figs 2b and 7b in Alonso-Herrero et al. 2000), which is likely to be associated with the star formation detected in the *Spitzer*/IRS spectrum. These regions of star formation, however, did not fall in the GTC/CanariCam slit.
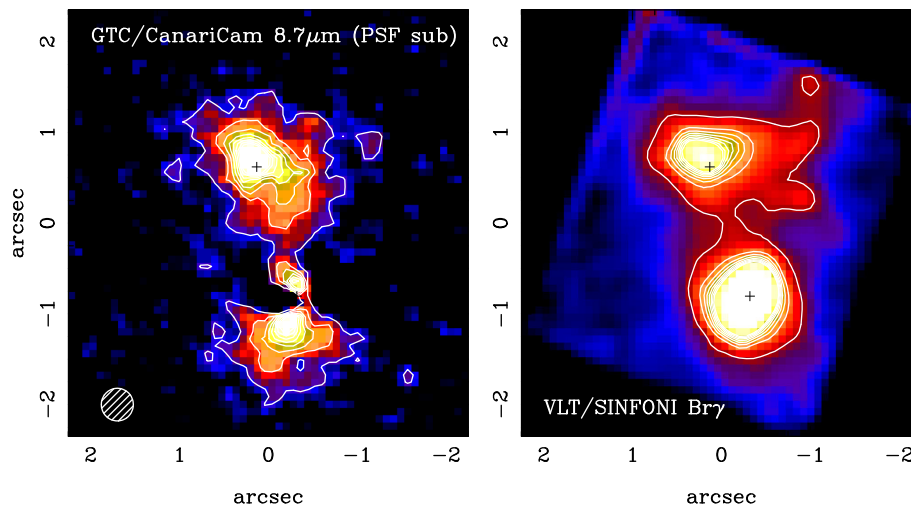
5.5 NGC 6240

NGC 6240 was previously imaged in the mid-IR using MIRLIN on the Keck II telescope (Egami et al. 2006) and VISIR on the VLT telescope (Asmus et al. 2014). The GTC/CanariCam 8.7 µm image of NGC 6240 (Fig. 4, top panel) shows mid-IR emission arising from both nuclei, with the southern nucleus being approximately five times brighter than the northern one (Table 5). The CanariCam image shows also diffuse emission around and in between the

nuclei. We detect extended emission in the central 4 arcsec ~ 1.9 kpc of the system. The core of the southern nucleus appears unresolved at the resolution of the CanariCam images (≤ 181 pc, FWHM), while the northern nucleus is resolved (see also Asmus et al. 2014) with an FWHM = 214 pc.

In order to study the extended mid-IR 8.7 µm emission in more detail, we subtracted the unresolved emission (PSF subtraction) from the southern nucleus of NGC 6240. We show the result in Fig. 9 compared with the VLT/SINFONI continuum-subtracted Brγ image from Engel et al. (2010). The latter emission in NGC 6240 is mostly believed to be tracing the starburst activity in this galaxy. We repixelated and smoothed the SINFONI image to match the pixel size and angular resolution of the CanariCam image.

As can be seen from this figure, there is a fairly good correspondence between both emissions, especially around the northern nucleus where the AGN contribution in the mid-IR is low (see below). There is also extended 8.7 µm emission to the south of the southern nucleus, which has also been detected in the near-IR continuum, Brγ, and other mid-IR wavelengths (Asmus et al. 2014). This again indicates that the extended 8.7 µm emission probes recent star formation activity. Some of the differences in morphologies might be attributed to the high extinction affecting the *K*-band emission in and around the nuclei (see fig. 9 in Engel et al. 2010). It is also interesting to note that the peaks of the Brγ line emission and the 8.7 µm emission around the northern nuclei are nearly coincident with the northern radio source (Beswick et al. 2001) to within one CanariCam pixel (~ 0.08 arcsec), while that is not the case for the peak of the 2 µm continuum (see Max, Canalizo & de Vries 2007; Engel et al. 2010). The radio source is believed to mark the position of the accreting black hole in the northern nucleus. At $\lambda > 2$ µm, the peaks coincide with the radio ones (Mori et al. 2014).

Fig. 4 (bottom panel) compares the CanariCam nuclear spectra with that observed through the *Spitzer*/IRS SL ~ 4 arcsec aperture, which contains the two nuclei (Armus et al. 2006). Both nuclear spectra show relatively bright emission from the 8.6 and 11.3 µm PAH features. The IRS spectrum and that of the southern nucleus also show bright molecular hydrogen lines H_2 at 8.025, 9.665, and

Figure 9. NGC 6240. Left-hand panel: GTC/CanariCam PSF-subtracted 8.7 µm (only unresolved emission from the southern nucleus was subtracted) in a square-root colour scale. The hatched circle is the FWHM of the PSF. The contours are the 8.7 µm emission with the lowest value as in Fig. 4 (top panel). Right-hand panel: VLT/SINFONI continuum-subtracted Brγ image in a square-root colour scale from Engel et al. (2010). We repixelated and smoothed the SINFONI image to match the pixel size and angular resolution of the CanariCam image. The contours are the Brγ emission with the lowest value set at the background level plus eight standard deviations (before smoothing the image).
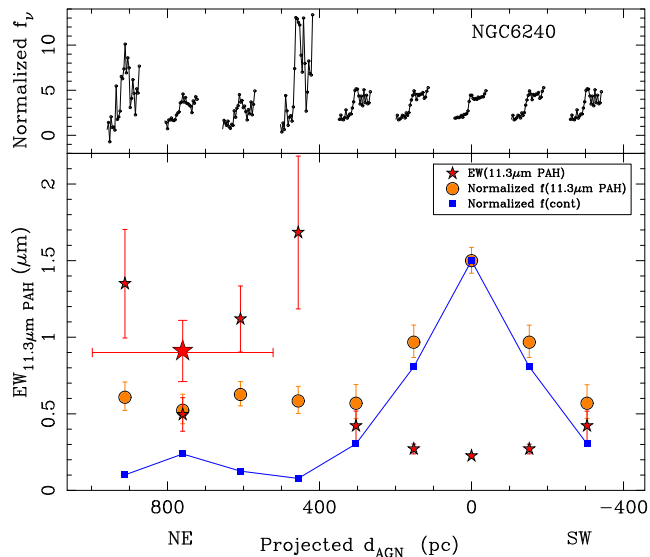
Figure 10. As Fig. 6, but for NGC 6240. The 0 position on the *x*-axis marks the location of the southern nucleus. The secondary peak in the local continuum at 11.25 µm at a projected distance of 760 pc to the north-east marks the approximate location of the northern nucleus of NGC 6240. The large star symbol is the measurement of the EW in the northern nucleus from the 0.52 arcsec × 1 arcsec spectrum (see also Table 6), shown as the horizontal error bar.

12.279 µm. The spatial profiles of Fig. 10 show that there is 11.3 µm PAH emission extending 3 arcsec ∼ 1.4 kpc along the slit. Both the local continuum at 11.25 µm and the 11.3 µm PAH feature peak at the southern nucleus, although the PAH emission appears to be slightly more extended. There is also extended PAH emission to the south-west of this nucleus where there is also detected extended emission in the 8.7 µm and Brγ images. Around the northern nucleus, the PAH emission is fainter than in the southern nucleus but it appears rather constant extending approximately 1.5 arcsec (∼700 pc) including the region between the two nuclei.

The spatial profile of the EW of the PAH feature shows a minimum (EW = 0.28 ± 0.02 µm) at the southern nucleus and a secondary minimum at the location of the northern nucleus (EW = 0.50 ± 0.11 µm). This clearly indicates the presence of a continuum, most likely associated with dust heated by the AGN in both nuclei, which is more dominant in the southern nucleus (see Mori et al. 2014, for a detailed analysis of the AGN IR emission of the southern nucleus). To the south-west of the southern nucleus and in the regions around the northern nucleus, the EW of the feature is similar to that measured in starburst galaxies, as is also the case for the *Spitzer*/IRS spectrum.

5.6 IRAS 17208−0014

The GTC/CanariCam 8.7 µm image of IRAS 17208−0014 (Fig. 5) shows emission extending over approximately 2 arcsec = 1.6 kpc. The morphology is similar to the Keck mid-IR 7 and 12 µm images (see Soifer et al. 2000) and the VLT/SINFONI Paα emission (Piqueras-López et al. 2012). The measured size of the nuclear region at 8.7 µm, which appears resolved in the CanariCam image, is 0.52 arcsec = 421 pc (FWHM), and therefore there is no clear evidence of the putative nuclear unresolved emission expected to be associated with the AGN.

The 2D GTC/CanariCam spectrum (see Fig. 5) shows extended PAH emission. The measured nuclear EW of the 11.3 µm feature

(EW = 0.56 ± 0.08 µm) shows that on scales of a few hundred pc the mid-IR emission of this galaxy is dominated by star formation. However, the lower nuclear value of the EW of the 11.3 µm PAH feature compared to the value measured in the IRS spectrum (EW = 0.90 ± 0.01 µm) indicates a higher continuum contribution there, which might be due to the AGN-produced mid-IR continuum. This is similar to findings for the nuclei of Arp 299 (see Table 6). Alternatively, the decreased nuclear EW in this galaxy could be due to an increased starburst continuum, as found in some purely star-forming nuclei (Tacconi-Garman et al. 2005; Díaz-Santos et al. 2010). Finally, the nuclear contribution to the *Spitzer*/IRS 11.3 µm PAH feature emission in IRAS 17208−0014 is 31 per cent, indicating that the emission of this feature is extended over at least a few kpc.

6 DISCUSSION

For this work, we selected six systems (eight galaxies) known to harbour an AGN and have intense star formation activity on nuclear and circumnuclear regions. We detected 11.3 µm PAH feature emission in all the galaxy nuclei (inner regions between 64 and 420 pc), except NGC 3690. Moreover, because some of them are LIRGs or ULIRGs, they tend to show more highly concentrated 11.3 µm PAH emission (i.e. star formation rate) than typical Seyferts (Esquej et al. 2014). This would be in line with the interpretation that local LIRGs may represent an IR-bright star-forming phase taking place prior to most of the AGN phase (Alonso-Herrero et al. 2013a). The galaxies in this work also have relatively high X-ray column densities, which may also be related to the material protecting the PAH molecules in the nuclear regions of AGN (Section 6.3). In what follows, we discuss in more detail the nuclear 11.3 µm PAH emission in local AGN.

6.1 Understanding the EW of the nuclear 11.3 µm PAH feature of Seyfert galaxies

The EW of the PAH features is routinely used to obtain a general classification of the dominant source of activity in galaxies (AGN versus star formation) in the near and mid-IR (see examples using the 3.3, 6.2, 7.7, and 11.3 µm PAH features in Imanishi & Dudley 2000; Spoon et al. 2007; Genzel et al. 1998; Hernán-Caballero & Hatziminaoglou 2011, respectively). It is also used to detect AGN not previously identified in the optical in LIRGs and ULIRGs (see e.g. Nardini et al. 2008; Alonso-Herrero et al. 2012). This is because generally high-metallicity star-forming galaxies show remarkably similar mid-IR spectra (Brandl et al. 2006), while the nuclear spectra of AGN are dominated by a strong continuum due to dust heated by the AGN. This results in AGN-dominated sources having much lower EWs of the PAHs than starburst galaxies. There is also both observational and theoretical evidence that PAH emission can be diminished/suppressed near (scales of a few pc) the ionizing sources in sites of intense star formation (e.g. Siebenmorgen et al. 2004; Tacconi-Garman et al. 2005; Tielens 2013).

A number of works using mid-IR spectra of AGN noted a tendency of decreasing EWs of PAHs with increasing hardness of the AGN radiation field and interpreted it as evidence of PAH destruction in the nuclear regions of AGN (see e.g. Wu et al. 2009; Sales et al. 2010). However, other interpretations for the decreased EW of PAH features in AGN include dilution from the intense mid-IR continuum produced by the AGN (see e.g. Lutz et al. 1998; Clavel et al. 2000) and reduction of the star formation activity from kpc scales to the nuclear regions of AGN (Hönig et al. 2010).
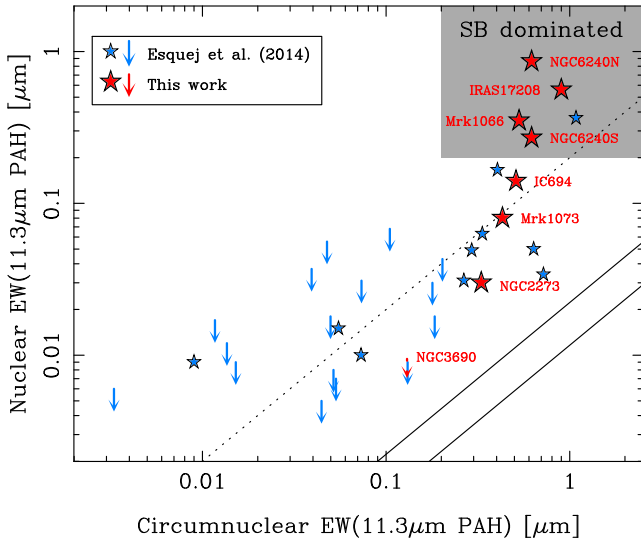
Figure 11. EW of the 11.3 μm PAH feature measured on nuclear scales (this work: red symbols, and Esquej et al. 2014: blue symbols) from 8–10 m class telescopes versus that on circumnuclear kpc scales with *Spitzer*/IRS SL spectra. The two solid lines represent the range of expected ratios for the case of uniform PAH emission taking into account the difference between ground-based slits (0.35–0.75 arcsec) and the IRS slit width. The dotted line represents the typical 0.2 ratio between the nuclear and circumnuclear PAH emission in RSA Seyferts (see Esquej et al. 2014). The shaded region shows the predicted EW for a starburst contribution ≥50 per cent to the observed mid-IR emission (see Hernán-Caballero & Hatziminaoglou 2011).

Owing to the high angular resolution of the CanariCam data, we showed in Section 5 that the nuclear EW of the 11.3 μm PAH feature varies with the distance from the AGN, always increasing at larger radial distances from the nucleus. This is similar to findings for Circinus and NGC 1808 using ground-based spatially resolved mid-IR spectroscopy (see Roche et al. 2006; Sales et al. 2013, respectively). We also demonstrated that since the 11.3 μm PAH flux peaks in the nuclear region, the minimum value of its EW in the nuclei of these AGN is due to an increased contribution from the AGN-produced continuum and not to PAH destruction (see also Tacconi-Garman & Sturm 2013, for the 3.3 μm PAH feature emission in the nuclear region of Centaurus A). Finally, in galaxies with a higher nuclear concentration of the star formation activity (Mrk 1066, NGC 6240, and IRAS 17208−0014, see last column in Table 5), the observed nuclear EW of the PAH feature is larger than those with smaller nuclear fractions of the PAH emission (NGC 2273, Mrk 1073, and NGC 3690). This simply reflects a higher contribution of the star formation activity with respect to the AGN emission.

In Fig. 11, we compare the EWs of the 11.3 μm PAH feature measured typically on hundreds of pc scales with *Spitzer*/IRS and nuclear scales with GTC/CanariCam. We also plotted in this figure data from Esquej et al. (2014) for Seyferts in the revised Shapley–Ames (RSA) galaxy catalogue (Maiolino & Rieke 1995) where the nuclear ground-based spectroscopy comes from 8–10 m telescopes and probes typically nuclear regions of 60 pc in size. The solid lines are the predictions for the nuclear EW in the presence of an AGN assuming that the PAH emission is distributed uniformly taking into account the range of slit sizes of the nuclear spectra and that of the *Spitzer*/IRS spectra. The dotted line represents the average value between nuclear and circumnuclear 11.3 μm PAH luminosities of 0.2 found for RSA Seyferts. Measurements above this line indicate

galaxies with strong nuclear star formation, as also expected from values of the EW if star formation contributes more than 50 per cent of the observed mid-IR emission. Since we selected the galaxies observed with CanariCam as having intense nuclear star formation, it is not surprising to see that the nuclear mid-IR emission in many of them is dominated by star formation when using the EW of the feature. It is also clear from this figure that unless there is a strong nuclear starburst, we should expect that the nuclear values of the EW are smaller than those measured on circumnuclear scales from *Spitzer*/IRS (Siebenmorgen & Krügel 2007).

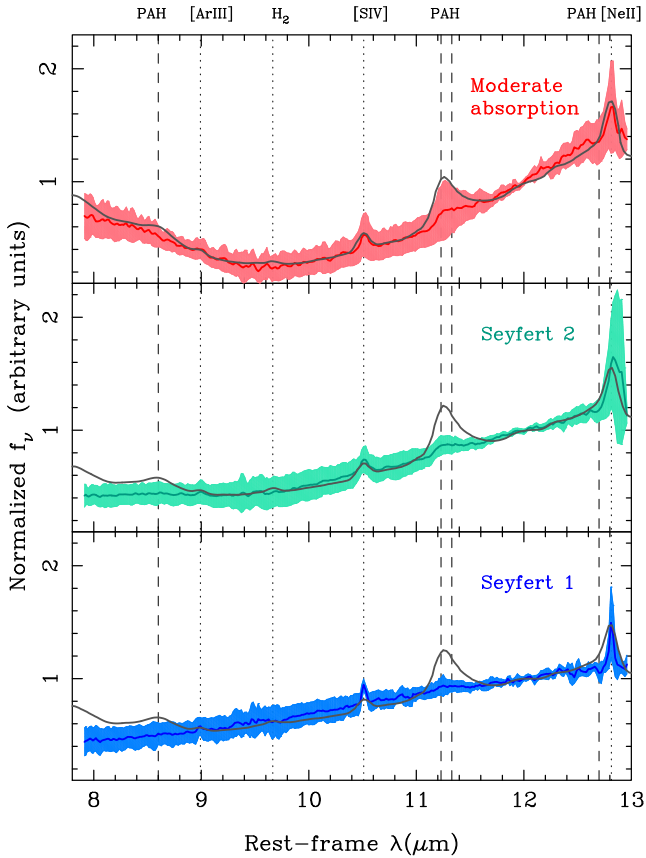### 6.2 Mid-IR spectra of Seyfert nuclei

In this section, we investigate further the detection of the 11.3 μm PAH feature in the close vicinity of AGN by constructing mean mid-IR spectra of Seyfert nuclei. We used the nuclear (typically the central 65 pc) mid-IR ground-based spectra of Seyfert galaxies in the RSA sample compiled by Esquej et al. (2014, their table 2), except for the two Seyferts with the 10 μm silicate feature in emission (NGC 2110 and NGC 7213) and NGC 1808 whose spectrum is dominated by star formation. We included the three galaxies (Mrk 1066, Mrk 1073, and NGC 2273) in our sample that are also in the RSA sample.

We divided the nuclear spectra in three categories, namely Seyfert 1, Seyfert 2, and Seyfert nuclei with silicate features in moderate absorption. We chose this last category because in these Seyfert 2 nuclei the silicate feature is likely to have a contribution from extended dust absorbing components in the host galaxy in addition to that due to the dusty torus (Deo et al. 2009; Alonso-Herrero et al. 2011; Goulding et al. 2012; González-Martín et al. 2013). These nuclei are generally in merger galaxies, galaxies with nuclear dust lanes, and/or highly inclined systems (see also Hönig et al. 2014). We combined the nuclear mid-IR spectra after normalizing them at 12 μm.

Fig. 12 shows the resulting mean mid-IR spectra of RSA Seyfert 1 and Seyfert 2 nuclei, and Seyfert nuclei with silicate features in moderate absorption compared to their corresponding circumnuclear *Spitzer*/IRS SL spectra. The nuclear spectra of Seyfert 1s and Seyfert 2s show similar mid-IR spectral indices (that is, ratio between 8 and 12 μm), consistent with the results of Hönig et al. (2010) comparing individual galaxies. However, the nuclear Seyfert 1 spectrum shows a flat or slightly in emission silicate feature whereas the Seyfert 2 shows the 10 μm feature slightly in absorption (see also Hönig et al. 2010).

The 11.3 μm PAH feature is detected in the average nuclear spectrum of the three types. Table 7 lists the mean and standard deviation of the EW of the 11.3 μm PAH feature for the average nuclear and IRS spectra for each type. We estimated the uncertainties of the EW in the combined spectra using bootstrap resampling. To do so, first we selected at random, and with replacement, a subset of the individual spectra used to build the composite. The size of the re-sample was equal to the size of the original set of spectra. We then obtained a composite spectrum for this subset and measured the EW of the feature. We repeated this routine 100 times to get the bootstrap distribution of the EW.

As expected, the nuclear EWs of all three types are smaller than those measured in the circumnuclear regions from the *Spitzer*/IRS spectra. This is due to the higher contribution of the mid-IR AGN continuum in the nuclear regions. The measured EW of the 11.3 μm PAH feature of Seyfert 1 and Seyfert 2 nuclei are similar, within the uncertainties. The average spectrum of the nuclei with the silicate feature in moderate absorption shows a slightly higher EW with a

Figure 12. Mid-IR spectra (normalized at 12 µm) of Seyfert 1 nuclei (bottom panel, blue line), Seyfert 2 nuclei (middle panel, green line), and Seyfert nuclei with silicate features in moderate absorption (top panel, red line) in the RSA sample. The shaded regions represent the 1σ dispersion. The three types clearly show nuclear 11.3 µm PAH emission. For comparison, the grey line for each type is the mean circumnuclear *Spitzer*/IRS SL spectra.

Table 7. EW of the 11.3 µm PAH feature in the spectra of Seyfert nuclei.

Class	No.	Nuclear Region (pc)	EW (µm)	*Spitzer*/IRS Region (pc)	EW (µm)
Seyfert 1	8	104	0.015 ± 0.007	650	0.192 ± 0.056
Seyfert 2	9	104	0.028 ± 0.016	720	0.228 ± 0.075
Moderate absorption	9	67	0.047 ± 0.038	625	0.233 ± 0.071

Notes. No. indicates the number of spectra combined and region the median value of the projected slit widths (in pc) of the nuclear and *Spitzer*/IRS spectra.

larger dispersion, but again consistent with those of Seyfert 1 and 2 nuclei. Since most of the nuclei with relatively deep silicate features are in highly inclined systems, there might be some contamination from star formation in the line of sight of the host galaxy. Additionally, in these systems, the silicate feature is likely to absorb the compact warm nuclear emission more than the diffuse PAH emission which arises from a much larger region. This suppresses the 11 µm continuum from the compact nuclear emission more than the 11.3 µm PAH emission and an increased EW is expected in these cases.

From this section and Section 6.1, we conclude that the decreasing EW of the 11.3 µm PAH features of local AGN going from circumnuclear scales (i.e. a few hundred pc probed by *Spitzer*/IRS
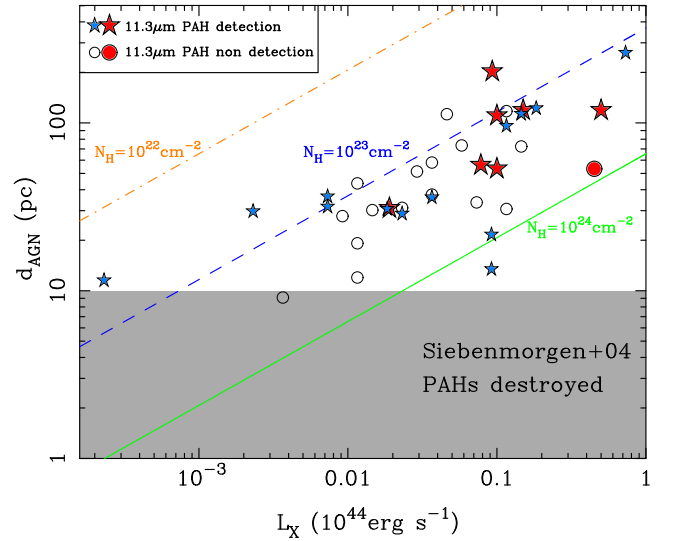
Figure 13. Diagram showing regions of PAH survival as a function of the distance from the AGN and the AGN X-ray luminosity according to the modelling of Voit (1992) and Miles et al. (1994). The lines of constant total column densities [lines from top to bottom $N_H(tot) = 10^{22}, 10^{23}, 10^{24}$ cm^{-2}] of the intervening material define the regions above which PAHs would be protected and not destroyed by the AGN radiation field. The shaded area shows the region where PAHs would not survive ($d_{AGN} \leq 10$ pc) according to the modelling of Siebenmorgen et al. (2004). Galaxies with a nuclear detection of the 11.3 µm PAH feature are shown as small and large star-like symbols for RSA galaxies from Esquej et al. (2014) and this work, respectively. Circles are galaxies with non-detections of the nuclear PAH feature. For the galaxies, the plotted X-ray luminosities are intrinsic (corrected for absorption) 2–10 keV luminosities and d_{AGN} are projected distances.

spectra) to nuclear scales of less than 100 pc (i.e. ground-based data obtained with 8–10 m class telescopes) is due to increased dilution from the AGN continuum (see also Ramos Almeida et al. 2014).

6.3 PAH survival in the vicinity of AGN?

The large molecules responsible for the long-wavelength PAH emission are expected to be less susceptible to destruction by X-ray photons produced by the AGN than those producing the 7.7 and 8.6 µm PAH emission (Smith et al. 2007). Therefore, the 11.3 µm PAH feature is likely to be more resistant to the AGN radiation field (see also Diamond-Stanic & Rieke 2010). In this section, we evaluate whether there is a dependence of the detection of this feature with the AGN luminosity and the projected distance of the star-forming regions from the AGN.

According to the modelling of Voit (1992), to detect PAH emission near AGN, the rate of evaporation of the PAH carriers due to the AGN radiation field has to be lower than the rate at which carbon gets reaccreted on to the PAHs. Voit (1992) quantified the time-scale needed for X-ray reabsorption by a 50-carbon molecule in terms of the distance of the PAH molecules from the AGN d_{AGN}, the AGN X-ray luminosity L_X, and the total hydrogen column density of the intervening material $N_H(tot)$:

$$\tau \sim 700 \, \text{yr} \left(\frac{N_H(tot)}{10^{22} \, \text{cm}^{-2}} \right)^{1.5} \left(\frac{d_{AGN}}{\text{kpc}} \right)^2 \left(\frac{L_X}{10^{44} \, \text{erg s}^{-1}} \right)^{-1}. \quad (1)$$

Fig. 13 summarizes graphically the predictions for PAH survival, assuming a time-scale for reaccretion of carbon on to a fractured PAH molecule of 3000 yr (see Voit 1992; Miles et al. 1994). We show lines of constant total hydrogen column densities as a

function of the AGN X-ray luminosity and distance from the AGN. Below these lines, PAH molecules might not survive the AGN radiation field. For a given column density, the more luminous the AGN is, the further away the PAH molecules ought to be in order to survive. Also, at a given AGN luminosity, higher column densities of the intervening material allow for smaller distances to the AGN of the star-forming regions where the PAH molecules could survive. We also show in this figure, for comparison, the predictions from Siebenmorgen et al. (2004) where the only dependence is the distance from the AGN, that is, PAH molecules would be destroyed at distances of less than approximately 10 pc from the AGN but survive at distances of more than 100 pc.

In Fig. 13, we also plotted the RSA Seyferts from Esquej et al. (2014) and the galaxies from this work. For the closest galaxies in the Esquej et al. (2014) sample (Circinus, NGC 4945, and NGC 5128), the distances from the AGN correspond to those probed by the *Spitzer*/IRS SL slit (see below). As can be seen from this figure, the majority of the galaxies with nuclear 11.3 μm PAH detections cluster around the $N_{\mathrm{H}}(\mathrm{tot}) = 10^{23}\ \mathrm{cm}^{-2}$ line and a few just around the $N_{\mathrm{H}}(\mathrm{tot}) = 10^{24}\ \mathrm{cm}^{-2}$ line.

The derived total column densities from fitting the nuclear IR emission of Seyfert nuclei with clumpy torus models are in this range (Ramos Almeida et al. 2009b, 2011; Lira et al. 2013). Independently, Hicks et al. (2009) derived typical column densities of $N_{\mathrm{H}} \sim 5 \times 10^{23}\ \mathrm{cm}^{-2}$ in the nuclear gas discs (radii of 30 pc) of Seyfert galaxies. Therefore, material in the dusty torus and/or gas disc has in principle sufficient column density to shield the PAH molecules from the AGN radiation field (see also Sales et al. 2013; Esquej et al. 2014). Moreover, Hicks et al. (2009) proposed that the molecular gas is mixed with the stellar population and is likely to be associated with the outer regions of the obscuring material (i.e. the torus). This scenario fits nicely with the physical scales where nuclear 11.3 μm PAH feature emission is detected in this work (inner few tens of pc) and with the relatively compact sizes inferred for the AGN tori (Ramos Almeida et al. 2009b, 2011; Tristram et al. 2009; Alonso-Herrero et al. 2011; Kishimoto et al. 2011; Burtscher et al. 2013).

We can also see from Fig. 13 that those nuclei where the 11.3 μm PAH feature is not detected do not lie in a particular region of the diagram. Rather, they are mostly located between the lines of constant $N_{\mathrm{H}} = 10^{23}$ and $10^{24}\ \mathrm{cm}^{-2}$, as those with nuclear detections of the feature. The question for the non-detections is whether they just do not have nuclear star formation or whether the PAH carriers have been destroyed. For Circinus and NGC 5128, which are the nearest galaxies in Esquej et al. (2014), the nuclear PAH emission is not clearly detected at distances of less 10 pc from ground-based spectroscopy (see Roche et al. 2006; González-Martín et al. 2013, respectively). The AGN of these two galaxies are embedded, as implied by the deep nuclear 9.7 μm silicate features. In these cases, it is not clear if the PAH molecules are destroyed or not. For Circinus Roche et al. (2006) concluded that the 11.3 μm PAH emission arises predominantly outside the regions affected by the large columns producing the strong nuclear absorption and further from the nucleus. For NGC 5128, Tacconi-Garman & Sturm (2013) detected nuclear 3.3 μm PAH emission, and therefore it is possible that the nuclear 11.3 μm PAH emission is embedded in the deep silicate feature.

One interesting case of non-detection of the nuclear 11.3 μm PAH feature is NGC 7213 (see Esquej et al. 2014; Ruschel-Dutra et al. 2014). The nuclear spectrum of this Seyfert 1 galaxy shows the silicate feature in emission. Ruschel-Dutra et al. (2014) fitted the mid-IR spectra with the Nenkova et al. (2008) models and derived

a very low hydrogen column density ($N_{\mathrm{H}} \sim 10^{18}\ \mathrm{cm}^{-2}$) compared with the typical values found in other Seyfert 1 and Seyfert 2 nuclei of $N_{\mathrm{H}} \sim 10^{23}$–$10^{24}\ \mathrm{cm}^{-2}$ (Ramos Almeida et al. 2009b, 2011, 2014; Lira et al. 2013; Sales et al. 2013, 2014; Ruschel-Dutra et al. 2014). For the AGN luminosity of NGC 7213 and the distance to the AGN probed by the high-angular-resolution mid-IR spectroscopy [$\log L(2-10\,\mathrm{keV}) = 42.1\ \mathrm{erg\,s^{-1}}$ and $d_{\mathrm{AGN}} = 20\ \mathrm{pc}$; see Esquej et al. 2014 and Ruschel-Dutra et al. 2014, the required column density to protect the PAH molecules would be a few times $10^{23}\ \mathrm{cm}^{-2}$ (see Fig. 13). The nuclear region of NGC 7213 may represent a case where there is not sufficient protecting material in the dusty torus. We note that this galaxy has a circumnuclear ring of star formation and some extended Hα emission (a few arcseconds) around the nucleus (see e.g. Storchi-Bergmann et al. 1996). However, in the nuclear region of NGC 7213, it is not clear if the Hα emission line is excited by nuclear star formation activity, by the AGN itself, or both.

Finally, some galaxies with a clear detection of the 11.3 μm PAH feature in the nuclear mid-IR spectrum (e.g. NGC 3783 and NGC 7469; see Hönig et al. 2010) do not show it in well-resolved interferometric observations probing much smaller physical scales (see Burtscher et al. 2013, and references therein). The second-generation instruments planned for the VLTI will provide more sensitive data and the possibility of image reconstruction. This will be useful to understand the behaviour of the nuclear 11.3 μm PAH feature of AGN on smaller physical scales than those probed by mid-IR spectroscopy on 8–10 m class telescopes.

7 CONCLUSIONS

We presented GTC/CanariCam Si-2 ($\lambda_{\mathrm{c}} = 8.7\ \mu\mathrm{m}$) imaging and $7.5-13\ \mu\mathrm{m}$ spectroscopy of six local systems (eight galaxies) known to host both an AGN and nuclear (regions of less than 500 pc) star formation activity. The main goal of this work was to explore the behaviour of the 11.3 μm PAH feature in the close vicinity of an AGN. The high angular resolution ($0.24-0.40$ arcsec) of the GTC/CanariCam observations allowed us to probe projected distances from the AGN between 30 and 210 pc, depending on the galaxy. We also included in our analysis the nuclear mid-IR spectra of 29 RSA galaxies presented by Esquej et al. (2014). We summarize our main conclusions as follows.

(i) We detected nuclear (inner ∼60–420 pc) and extended (a few hundred pc from the AGN) 11.3 μm PAH feature emission in all the systems observed with GTC/CanariCam. The only exception is the nuclear region (inner 0.5 arcsec ∼ 100 pc) of NGC 3690. However, the upper limit of the EW of the feature is compatible with expectations from the comparison of its nuclear star formation rate with that of its companion galaxy IC 694.

(ii) We measured GTC/CanariCam nuclear EW of the 11.3 μm PAH feature ranging from values indicating AGN-dominated nuclear mid-IR emission (NGC 3690, NGC 2273, and Mrk 1073) to intermediate cases (IC 694) to starburst-dominated nuclear mid-IR emission (both nuclei of NGC 6240, Mrk 1066, and IRAS 17208−0014).

(iii) The GTC/CanariCam spatially resolved spectroscopy shows that the 11.3 μm PAH feature emission peaks in the galaxy nuclei with the EW of the feature increasing further away from the AGN. At projected distances from the AGN of a few hundred pc, the EW of the feature reaches values consistent with those of star-forming galaxies.

(iv) The nuclear EW of the 11.3 µm PAH feature are always lower than those measured from *Spitzer*/IRS spectra probing circumnuclear regions, which are typically factors of 7 larger in size than the nuclear regions. We explained the reduced nuclear EW of the 11.3 µm PAH feature as due to an increased AGN continuum contribution in the nuclear regions rather than destruction of the PAH carriers by the AGN radiation.

(v) We investigated the survival of the PAH molecules responsible for the 11.3 µm PAH feature. We found no evidence of complete destruction of the molecules responsible for this PAH feature in the nuclear regions of AGN at least to distances as close as 10 pc from the nucleus.

For Seyfert-like AGN luminosities and distances to the nucleus probed by high-angular-resolution (0.2–0.4 arcsec) mid-IR measurements, the implied minimum column densities of the intervening material needed to protect the molecules responsible for the 11.3 µm PAH feature are $N_H = 10^{23}$ cm^{-2} (see also Esquej et al. 2014). Current modelling of the nuclear IR emission of Seyfert galaxies with clumpy torus models indicates that the compact torus is able to provide such column densities, even for most type 1 AGN (Ramos Almeida et al. 2009b, 2011; Alonso-Herrero et al. 2011). Likewise, column densities $N_H \sim 5 \times 10^{23}$ cm^{-2} are derived for the nuclear gas discs of nearby AGN (Hicks et al. 2009).

We conclude that the 11.3 µm PAH feature can be used to probe nuclear star formation activity for Seyfert-like AGN luminosities and at least to distances to the AGN of 10 pc, assuming that the AGN contribution to the excitation of the 11.3 µm PAH feature is small or negligible.

REFERENCES

Aitken D. K., Roche P. F., 1985, MNRAS, 213, 777
Alexander D. M., Hickox R. C., 2012, New Astron. Rev., 56, 93
Alonso-Herrero A., Rieke G. H., Rieke M. J., Scoville N. Z., 2000, ApJ, 532, 845
Alonso-Herrero A., Colina L., Packham C., Díaz Santos T., Rieke G. H., Radomski J. T., Telesco C., 2006, ApJ, 625, L83
Alonso-Herrero A. et al., 2009, ApJ, 697, 660
Alonso-Herrero A. et al., 2011, ApJ, 736, 82
Alonso-Herrero A., Pereira-Santaella M., Rieke G. H., Rigopoulou D., 2012, ApJ, 744, 2
Alonso-Herrero A., Pereira-Santaella M., Rieke G. H., Diamond-Stanic A. M., Wang Y., Hernán-Caballero A., Rigopoulou D., 2013a, ApJ, 765, 78
Alonso-Herrero A. et al., 2013b, ApJ, 779, L14
Armus L. et al., 2006, ApJ, 640, 204
Arribas S., Colina L., 2003, ApJ, 591, 791
Asmus D., Hönig S. F., Gandhi P., Smette A., Duschl W. J., 2014, MNRAS, 439, 1648
Awaki H., Terashima Y., Higaki Y., Fukazawa Y., 2009, PASJ, 61, S317
Barbosa F. K. B., Storchi-Bergmann T., Cid Fernandes R., Winge C., Schmitt H., 2006, MNRAS, 371, 170
Beswick R. J., Pedlar A., Mundell C. G., Gallimore J. F., 2001, MNRAS, 325, 151
Brandl B. R. et al., 2006, ApJ, 653, 1129
Burtscher L. et al., 2013, A&A, 558, A149
Cid Fernandes R., Heckman T., Schmitt H., González Delgado R. M., Storchi-Bergmann T., 2001, ApJ, 558, 81
Clavel J. et al., 2000, A&A, 357, 839
Davies R. I., Müller Sánchez F., Genzel R., Tacconi L. J., Hicks E. K. S., Friedrich S., Sternberg A., 2007, ApJ, 671, 1388
Della Ceca R. et al., 2002, ApJ, 581, L9
Deo R. P., Richards G. T., Crenshaw D. M., Kraemer S. B., 2009, ApJ, 705, 14
Diamond-Stanic A. M., Rieke G. H., 2010, ApJ, 724, 140
Diamond-Stanic A. M., Rieke G. H., 2012, ApJ, 746, 168
Díaz-Santos T., Alonso-Herrero A., Colina L., Packham C., Radomski J., Telesco C., 2008, ApJ, 684, 211
Díaz-Santos T., Alonso-Herrero A., Colina L., Packham C., Levenson N. A., Pereira-Santaella M., Roche P. F., Telesco C., 2010, ApJ, 711, 328
Egami E., Neugebauer G., Soifer B. T., Matthews K., Becklin E. E., Ressler M. E., 2006, AJ, 131, 1253
Engel H. et al., 2010, A&A, 524, A56
Esquej P. et al., 2014, ApJ, 780, 86
Ferruit P., Wilson A. S., Mulchaey J., 2000, ApJS, 128, 139
Genzel R. et al., 1998, ApJ, 498, 579
González Delgado R. M., Heckman T., Leitherer C., 2001, ApJ, 546, 845
González-Martín O., Masegosa J., Márquez I., Guainazzi M., 2009, ApJ, 704, 1570
González-Martín O. et al., 2013, A&A, 553, A35
Goulding A. D., Alexander D. M., Bauer F. E., Forman W. R., Hickox R. C., Jones C., Mullaney J. R., Trichas M., 2012, ApJ, 755, 5
Guainazzi M., Matt G., Perola G. C., 2005, A&A, 444, 119
Helou G. et al., 2004, ApJS, 154, 253
Hernán-Caballero A., Hatziminaoglou E., 2011, MNRAS, 414, 500
Hicks E. K. S., Davies R. I., Malkan M. A., Genzel R., Tacconi L. J., Müller Sánchez F., Sternberg A., 2009, ApJ, 696, 448
Hönig S., Kishimoto M., Gandhi P., Smette A., Asmus D., Duschl W., Polletta M., Weigelt G., 2010, A&A, 515, 23
Hönig S., Gandhi P., Asmus D., Mushotzky R. F., Antonucci R., Ueda Y., Ichikawa K., 2014, MNRAS, 438, 647

Hopkins P. F., 2012, MNRAS, 420, L8

Hopkins P. F., Quataert E., 2010, MNRAS, 407, 1529

Houck J. R. et al., 2004, ApJS, 154, 18

Imanishi M., Dudley C. C., 2000, ApJ, 545, 701

Kawakatu N., Wada K., 2008, ApJ, 681, 73

Kishimoto M., Hönig S. F., Antonucci R., Millour F., Tristram K. R. W., Weigelt G., 2011, A&A, 536, 78

Komossa S., Burwitz V., Hasinger G., Predehl P., Kaastra J. S., Ikebe Y., 2003, ApJ, 582, L15

Laurent O., Mirabel I. F., Charmandaris V., Gallais P., Madden S. C., Sauvage M., Vigroux L., Cesarsky C., 2000, A&A, 359, 887

Lebouteiller V., Barry D. J., Spoon H. W. W., Bernard-Salas J., Sloan G. C., Houck J. R., Weedman D. W., 2011, ApJS, 196, 8

Lira P., Videla L., Wu Y., Alonso-Herrero A., Alexander D., Ward M., 2013, ApJ, 764, 59

Lutz D., Spoon H. W. W., Rigopoulou D., Moorwood A. F. M., Genzel D., 1998, ApJ, 505, L103

Maiolino R., Rieke G. H., 1995, ApJ, 454, 95

Maiolino R., Ruiz M., Rieke G. H., Keller L. D., 1995, ApJ, 446, 561

Marinucci A., Bianchi S., Nicastro F., Matt G., Goulding A. D., 2012, ApJ, 748, 130

Max C. E., Canalizo G., de Vries W. H., 2007, Science, 316, 1877

Miles J. W., Houck J. R., Hayward T. L., 1994, ApJ, 425, L37

Mori T. I. et al., 2014, PASJ, submitted (arXiv:1406.7780)

Nardini E., Risaliti G., Salvati M., Sani E., Imanishi M., Marconi A., Maiolino R., 2008, MNRAS, 385, L130

Nenkova M., Sirocky M. M., Nikutta R., Ivezić Z., Elitzur M., 2008, ApJ, 685, 160

Packham C., Radomski J. T., Roche P. F., Aitken D. K., Perlman E., Alonso-Herrero A., Colina L., Telesco C. M., 2005, ApJ, 618, L17

Peeters E., Spoon H. W. W., Tielens A. G. G. M., 2004, ApJ, 613, 986

Piqueras-López J., Colina L., Arribas S., Alonso-Herrero A., Begregal A. G., 2012, A&A, 546, A64

Quillen A. C., Alonso-Herrero A., Rieke M. J., Rieke G. H., Ruiz M., Kulkarni V., 1999, ApJ, 527, 696

Radomski J. T., Piña R. K., Packham C., Telesco C. M., De Buizer J. M., Fisher R. S., Robinson A., 2003, ApJ, 587, 117

Raimann D., Storchi-Bergmann T., González Delgado R. M., Cid Fernandes R., Heckman T., Leitherer C., Schmitt H., 2003, MNRAS, 339, 772

Ramos Almeida C., Pérez García A. M., Acosta-Pulido J. A., 2009a, ApJ, 694, 1379

Ramos Almeida C. et al., 2009b, ApJ, 702, 1127

Ramos Almeida C. et al., 2011, ApJ, 731, 92

Ramos Almeida C. et al., 2014, MNRAS, submitted

Riffel R. A., Storchi-Bergmann T., 2011, MNRAS, 411, 469

Riffel R. A., Storchi-Bergmann T., Nagar N. M., 2010, MNRAS, 404, 166

Roche P. F., Aitken D. K., Smith C. H., Ward M. J., 1991, MNRAS, 248, 606

Roche P. F., Packham C., Telesco C. M., Radomski J. T., Alonso-Herrero A., Aitken D. K., Colina L., Perlman E., 2006, MNRAS, 367, 1689

Ruschel-Dutra D., Pastoriza M., Riffel R., Sales D. A., Winge C., 2014, MNRAS, 438, 3434

Sales D. A., Pastoriza M. G., Riffel R., 2010, ApJ, 725, 605

Sales D. A., Pastoriza M. G., Riffel R., Winge C., 2013, MNRAS, 429, 2634

Sales D. A., Ruschel-Dutra D., Pastoriza M. G., Riffel R., Winge C., 2014, MNRAS, 441, 630

Sanders D. B., Mazzarella J. M., Kim D.-C., Surace J. A., Soifer B. T., 2003, AJ, 126, 1607

Sani E. et al., 2012, MNRAS, 424, 1936

Shi Y. et al., 2007, ApJ, 669, 841

Siebenmorgen R., Krügel E., 2007, A&A, 461, 445

Siebenmorgen R., Krügel E., Spoon H. W. W., 2004, A&A, 414, 123

Smith D. A., Herter T., Haynes M. P., Beichman C. A., Gautier T. N., 1996, ApJS, 104, 217

Smith J. D. et al., 2007, ApJ, 656, 770

Soifer B. T. et al., 2000, AJ, 119, 509

Spoon H. W. W., Marshall J. A., Houck J. R., Elitzur M., Hao L., Armus L., Brandl B. R., Charmandaris V., 2007, ApJ, 654, 49

Storchi-Bergmann T., Rodriguez-Ardila A., Schmitt H. R., Wilson A. S., Baldwin J. A., 1996, ApJ, 472, 83

Tacconi-Garman L. E., Sturm E., 2013, A&A, 551, A139

Tacconi-Garman L. E., Sturm E., Lehnert M., Lutz D., Davies R. I., Moorwood A. F. M., 2005, A&A, 432, 91

Telesco C. M. et al., 2003, in Iye M., Moorwood A. F. M., eds, Proc. SPIE Conf. Ser. Vol. 4841, Instrument Design and Performance for Optical/Infrared Ground-based Telescopes. SPIE, Bellingham, p. 913

Tielens A. G. G. M., 2013, Rev. Mod. Phys., 85, 1021

Tommasin S., Spinoglio L., Malkan M. A., Fazio G., 2010, ApJ, 709, 1257

Tristram K. R. W. et al., 2009, A&A, 502, 67

Veilleux S., Goodrich R. W., Hill G. J., 1997, ApJ, 477, 631

Voit G. M., 1992, MNRAS, 258, 841

Vollmer B., Beckert T., Davies R. I., 2008, A&A, 491, 441

Wada K., Norman C. A., 2002, ApJ, 566, L21

Wild V., Heckman T., Charlot S., 2010, MNRAS, 405, 933

Wu Y., Charmandaris V., Huang J., Spinoglio L., Tommasin S., 2009, ApJ, 701, 658

This paper has been typeset from a TEX/LATEX file prepared by the author.